

Canonical Variational Theory for Enzyme Kinetics with the Protein Mean Force and Multidimensional Quantum Mechanical Tunneling Dynamics. Theory and Application to Liver Alcohol Dehydrogenase

Cristóbal Alhambra, José Corchado, Maria Luz Sánchez, Mireia Garcia-Viloca, Jiali Gao,* and Donald G. Truhlar*

Department of Chemistry and Supercomputer Institute, University of Minnesota, Minneapolis, Minnesota 55455-0431

Received: May 30, 2001; In Final Form: July 30, 2001

We present a theoretical framework for the calculation of rate constants of enzyme-catalyzed reactions that combines variational optimization of the dynamical bottleneck for overbarrier reactive events and multidimensional quantum mechanical tunneling dynamics for through-barrier reactive events, both in the presence of the protein environment. The theory features a two-zone, three-stage procedure called ensemble-averaged variational transition state theory with multidimensional tunneling (EA-VTST/MT) with the transmission coefficient based on the equilibrium secondary-zone (ESZ) approximation for including the effects of the protein on a catalytic reaction center, called the primary zone. The dynamics is calculated by canonical variational theory with optimized multidimensional tunneling contributions, and the formalism allows for Boltzmann averaging over an ensemble of reactant and transition state conformations. In the first stage of the calculations, we assume that the generalized transition states can be well described by a single progress coordinate expressed in primary-zone internal coordinates; in subsequent steps, the transmission coefficient is averaged over a set of primary-zone reaction paths that depend on the protein configuration, and each reaction path has its own reaction coordinate and optimized tunneling path. We also present a simpler approximation to the transmission coefficient that is called the static secondary-zone (SSZ) approximation. We illustrate both versions of this method by carrying out calculations of the reaction rate constants and kinetic isotope effects for oxidation of benzyl alcoholate to benzaldehyde by horse liver alcohol dehydrogenase. The potential energy surface is modeled by a combined generalized hybrid orbital/quantum mechanical/molecular mechanical/semiempirical valence bond (GHO-QM/MM/SEVB) method. The multidimensional tunneling calculations are microcanonically optimized by employing both the small-curvature tunneling approximation and version 4 of the large-curvature tunneling approximation. We find that the variation of the protein mean force as a function of reaction coordinate is quantitatively significant, but it does not change the qualitative conclusions for the present reaction. We obtain good agreement with experiment for both kinetic isotope effects and Swain–Schaad exponents.

1. Introduction

The significant role of quantum mechanical dynamical effects in enzyme catalysis is receiving considerable attention in recent years.^{1–32} We especially note the considerable experimental evidence for important tunneling effects in several enzyme systems that has been presented by Klinman, Davidson, and Scrutton and co-workers.^{2–12,25–30} It also has been recently shown that quantization of bound vibrational motions, especially the inclusion of zero point energy, can have a significant effect on rate constants and free energies of activation of enzyme reactions.^{15,21,23,32} Although considerable progress has been made in incorporating quantum mechanical dynamical effects into small-molecule reactions where there is only a single important conformation of the transition state, the incorporation of such effects into enzyme kinetics requires a method to average such effects over a myriad of conformations.^{33,34} This is most easily accomplished by computing a potential of mean force (PMF)^{15,21–23,35–51} along a reactive progress variable, and the present article presents a practical formalism for combining such

a calculation with multidimensional semiclassical transmission coefficient for incorporating the effects of quantized molecular vibrations and quantum mechanical tunneling. The method presented here incorporates elements from three previous papers in our group,^{21–23} but it combines them in a new way that allows for a more satisfactory inclusion of enzyme conformational and entropic effects. In particular, our previous calculations^{21,22} on enzyme reaction rates employed a PMF calculation for the sole purpose of generating a transition state ensemble of bath configurations, whereas the present method uses the PMF calculation to compute a free energy difference between reactants and generalized transition states for the rate constant calculation.

The dynamical formulation employed for tunneling in this paper is called semiclassical because it approximates the quantum mechanical transmission probabilities in terms of imaginary action integrals, as in the Wentzel–Kramers–Brillouin (WKB) approximation;⁵² such a treatment is customarily called semiclassical because it involves using classical variables (or their analytic continuation to complex momenta) to approximate quantum mechanical dynamics.⁵³ An intermedi-

* Corresponding authors. E-mail: gao@chem.umn.edu and truhlar@umn.edu.

ate stage in the incorporation of quantum mechanical effects is to quantize bound vibrations but neglect tunneling and other quantum effects on the unbound reaction coordinate. This dynamical level will be called quasiclassical (QC) by analogy to some methods used for gas-phase reactions.^{54–56} We have explained our usage of “semiclassical” and “quasiclassical” in the Introduction because their multiple meanings sometimes cause confusion. When we use these terms below, they have the meanings discussed here.

Liver alcohol dehydrogenase (LADH) catalyzes the reversible transformation of an alcohol to an aldehyde. It functions through a ternary complex of the enzyme itself (which is a dimer), a nicotinamide adenine dinucleotide (NAD⁺) coenzyme, and the substrate.^{57,58} We have previously presented a successful multidimensional semiclassical treatment of the kinetic isotope effects (KIEs) in this reaction using the preliminary theory of refs 21 and 22, and in the present paper, we illustrate the new, more complete method presented here by applying it to the same problem.

The method used here involves three stages. Stage 1 begins with a statistical mechanical calculation of the classical mechanical potential of mean force on the reaction progress coordinate, and this is then augmented by an estimate of the quantum mechanical vibrational free energy as a function of the progress coordinate. From these calculations, we calculate both a classical mechanical (CM) and a quasiclassical (QC) rate constant estimate. The classical mechanical simulation of stage 1 is carried out with the molecular dynamics (MD) module of the CHARMM computer program.⁵⁹

Stages 2 and 3 consist formally of calculating transmission coefficients^{36,37,41,43,60–66} for transition state configurations sampled on the basis of the stage-1 calculations.

Stage 2 involves semiclassical reaction path calculations for a subsystem called the primary zone in the presence of frozen configurations of the secondary zone (also called the bath); the secondary-zone configurations are taken from a transition state ensemble optimized either classically or quasiclassically in stage 1. This is called the static secondary-zone (SSZ) approximation. The secondary zone can include part of the substrate and coenzyme, if any, and it includes most or all of the protein and solvent. The semiclassical reaction path calculations are carried out with the CHARMMRATE module⁶⁷ of CHARMM, which interfaces CHARMM to the POLYRATE^{68,69} computer program.

The phenomenological free energy of activation may be divided into a substantial part and a nonsubstantial part.⁷⁰ The former is the part arising from a quasithermodynamic treatment of the reactant and transition state. In the present article, it is calculated first classically and then quasiclassically as the difference between the free energy of the transition state with a classical reaction coordinate separated out and the free energy of the reactant. The nonsubstantial free energy is extrathermodynamic; it results entirely from the part of the transmission coefficient that is not equivalent to finding a better transition state with a separable classical reaction coordinate. The transmission coefficient is based on sampling over a set of more physical reaction coordinates than the single reaction coordinate used in stage 1, and therefore—in addition to tunneling—it also includes a correction for recrossing of the original, less physical transition state. This correction could be considered to be a nonsubstantial (extrathermodynamic) dynamical correction factor; however, because it is based on an average over transition state calculations, it can also be considered to contribute to the

substantial free energy of activation of a virtual transition state, and we will include it in our stage-2 and stage-3 QC rate constants.

The free energy of the secondary zone is included in the stage-1 free energy of activation but not in the calculation of the stage-2 transmission coefficient. In stage 3, we calculate the free energy of the secondary zone by free energy perturbation theory along the minimum-energy paths of stage 2. This allows us to include the secondary-zone free energy in the transmission coefficient. This is called the equilibrium-secondary-zone (ESZ) approximation.

The semiclassical transmission coefficients of stages 2 and 3 are calculated by canonical variational theory^{64,71–77} (which is abbreviated CVT and which is a short name for canonical variational transition state theory) with microcanonical optimized multidimensional tunneling⁷⁸ (μ OMT) and, in stage 2, the ground-state-transmission-coefficient⁷² approximation or, in stage 3, the zero-order canonical-mean-shape⁴⁵ approximation. (The former was originally developed for the case in which there is no thermal bath, and the latter is for use when the primary system is described by a potential of mean force in a thermal bath.) The μ OMT approximation involves a variational choice⁷⁸ between small-curvature tunneling^{68,79} (SCT) and large-curvature tunneling^{78,80} (LCT). Thus, it allows for (but does not require) large-curvature tunneling paths in which the tunneling path differs from the minimum-energy reaction path by more than a zero point vibrational amplitude or the radius of curvature of the isoinertial reaction path or both.^{81,82} Reduced-dimensionality calculations^{83,84} have shown that such tunneling paths are sometimes essential for describing hydride transfer from carbon to NAD⁺ in bimolecular reactions. (The physical characteristics of small- and large-curvature tunneling paths are reviewed with illustrations in papers published elsewhere.^{85,86}) In the present work, we applied the well-established centrifugal-dominant small-curvature algorithm described elsewhere^{68,79} for small-curvature tunneling, and we applied the recently developed large-curvature, version-4 algorithm⁸⁰ to examine the possible importance of large-curvature tunneling for the LADH-catalyzed reaction. (The four versions of the large-curvature tunneling approximation that we have proposed in previous work differ only in technical ways that need not concern the general reader, with the most important differences having to do with the way that the effective Hamiltonian is treated near the boundary between the vibrationally adiabatic region, close to the minimum-energy path, of the potential energy surface and the nonadiabatic region where the tunneling path exhibits extensive corner cutting. We believe that the version-4 algorithm is more robust than the three previous algorithms, especially for low-energy tunneling in systems with anharmonic low-frequency modes such as occur in the present application, and it is our current standard method for large-curvature tunneling.)

Section 2 presents the dynamical theory. Section 3 reviews the experimental background on the LADH system and summarizes the potential QM/MM method that we used to model its potential energy function. Section 4 presents the three-stage calculations that we carried out. Sections 5 and 6 present results and discussion, respectively.

2. Dynamical Theory

Practical methods for applying the CVT/ μ OMT semiclassical method to include quantum mechanical dynamical effects in the treatment of gas-phase,^{71–74,76–79} gas–solid interface,^{75,87} and liquid-phase reactions^{23,45,88–90} are well developed and explained elsewhere. Parallel to this development, classical

molecular dynamics and free energy simulation techniques have been applied to condensed-phase and enzymatic reactions.^{36–51,91–95} However, new techniques that combine quantum mechanical or semiclassical dynamics and statistical mechanical simulations are required to include quantum mechanical dynamical effects in reaction rate calculations involving biopolymers; such applications were presented in two recent papers,^{21,22} which presented a two-stage algorithm that may be considered a preliminary version of the static-secondary-zone (SSZ) approximation, and the present paper gives the more complete SSZ approximation and introduces an improved three-stage algorithm, to be called the equilibrium secondary-zone (ESZ) approximation. The present paper formulates the rate constant within the SSZ and ESZ approximation in terms of a configurationally averaged transmission coefficient. The SSZ transmission coefficient is based on the static potential field of the secondary zone, i.e., the static secondary-zone force, and the ESZ transmission coefficient includes the equilibrium free energy of the secondary zone, i.e., the equilibrium secondary-zone potential of mean force.

The dynamics calculations proceed in three stages. Stage 1 includes a simulation in which all atoms of the entire N -atom system are treated on an equal footing, whereas in step 2 of stage 1 and in stages 2 and 3, the N -atom system is partitioned into N_1 primary-zone atoms and N_2 secondary-zone atoms, where $N_2 = N - N_1$. Step 1 of the first stage is classical mechanical (CM), whereas step 2 of stage 1 is quasiclassical (QC); stage 2 is semiclassical (SC) for the primary zone and classical for the secondary zone, and stage 3 is again SC for the primary zone and CM for the secondary zone, but with an improvement in the CM part.

The objective in stage 1 is to determine the potential of mean force (PMF), $W(z)$, along a progress coordinate defined by

$$z = r_{\text{HD}} - r_{\text{HA}} \quad (1)$$

where r_{HD} and r_{HA} are distances between the migrating hydride atom and the donor carbon atom (D) of benzyl alcoholate and the acceptor carbon atom (A) of NAD^+ . The classical mechanical PMF, to be called $W^{\text{CM}}(T, z)$ is determined using the umbrella sampling technique^{91–95} to obtain the probability density of configurations, $\rho(T, z)$ with distinguished coordinate value z at temperature T . Then

$$W^{\text{CM}}(T, z) = -RT \ln \rho(T, z) + W_o \quad (2)$$

where R is the gas constant, T is temperature, and W_o is a normalization constant. In practice, a series of simulations is carried out for a sequence of regions (or windows) along z by a restraining or biasing potential added to the potential energy function. The biasing potential is chosen to allow adequate overlap between windows, and the effect of the biasing potential is removed by statistical analysis to yield $\rho(T, z)$. There are no other restraints or constraints applied to the protein–solvent system except for the boundary potential during the umbrella sampling calculations. The probability density in each window is collected at a bin width of 0.01 Å, half of which is the statistical error on the precision of the reaction coordinate. This part of the calculation can be carried out using purely classical mechanics,^{21,22,91–94} which is often used for simulation studies of enzymatic reactions reported in the literature, or one can include quantum mechanical vibrational energy in $W^{\text{CM}}(T, z)$.²³ In the former case, the stage-1 PMF is labeled CM, and in the latter case, it is labeled QC.

We calculate the CM PMF for the isotopically unsubstituted case. Note that the CM PMF automatically includes all forms of nuclear-motion free energy except for that due to mode z . In particular, it includes conformational free energy due to multiple torsional minima and due to large-amplitude motions of the protein, and it includes anharmonic vibrational and librational free energies of the primary and secondary zones. It is well-known that $W^{\text{CM}}(T, z)$ is independent of mass.⁹⁵ Thus, $W^{\text{CM}}(T, z)$, although computed for the isotopically unsubstituted case, is equally applicable to the isotopically substituted cases. However, the contributions to $W^{\text{CM}}(T, z)$ of specific motions (especially individual localized modes of vibration and libration) do depend on masses. We include quantum effects only on the $3N_1 - 7$ highest-frequency vibrational modes of the primary zone in a hypersurface orthogonal to z , and when we do so, we add the difference between the quantum mechanical and classical mechanical free energies of those modes for a single consistent set of isotope-dependent effective frequencies. The QC PMF is approximated by adding a quantal correction to the CM PMF; the quantal correction is based on a harmonic approximation to the vibrational free energy of the primary zone, but it implicitly includes some anharmonicity because we use average effective frequencies based on instantaneous normal modes rather than true harmonic frequencies based on a single local minimum of the potential energy. The relationship between the QC PMF and the CM PMF is

$$W^{\text{QC}}(T, z) = W^{\text{CM}}(T, z) + \Delta W_{\text{vib}}(T, z) \quad (3)$$

where $\Delta W_{\text{vib}}(T, z)$ is given in ref 23 and represents the difference between the quantal and classical effective-harmonic vibrational free energies for $3N_1 - 7$ vibrational modes orthogonal to the reaction coordinate for the isotopic case of interest. We note that the nominal harmonic approximation in $\Delta W_{\text{vib}}(T, z)$ in ref 23 and here is not an intrinsic limitation. For example, one could use Feynman path integrals^{15,96–98} to evaluate $\Delta W_{\text{vib}}(T, z)$, including anharmonicity or to directly include quantum effects in the transition state calculation, replacing the classical mechanical calculation employed here, but we will not pursue such approaches in the present article. (Methods based on path integrals are compared to the kind of treatment used here in a recent review.⁹⁷)

The constraint that the modes included in $\Delta W_{\text{vib}}(T, z)$ are orthogonal to the reaction coordinate is achieved by a projection operator. The method used for evaluating $\Delta W_{\text{vib}}(T, z)$ in the present work is the same as those presented in ref 23, except for the projection operator. In the present work, we use a projection operator⁹⁹ based on Wilson B matrices to remove the rectilinear direction orthogonal to a hypersurface of constant z . Details of the projection operator are provided in the Appendix.

Generalized transition state theory corresponds to computing the equilibrium one-way flux through a dividing hypersurface separating reactants from products. We will define this dividing hypersurface by $z = z_*$, where z_* is a constant. In principle, z_* is a function of temperature, i.e., $z_*(T)$, but for simplicity, we will not include this dependence in the notation. The best choice for z_* would be the value of z that maximizes $W^{\text{QC}}(T, z)$. To find this value of z , one would compute $W^{\text{QC}}(T, z)$ as a function of z and fit the values near the maximum to a parabola or high-order function to identify z_* . A less expensive option that does not require calculating $\Delta W_{\text{vib}}(T, z)$ as a function of z is to compute only $W^{\text{CM}}(T, z)$ as a function of z and define z_* as the value of z that maximizes $W^{\text{CM}}(T, z)$. To evaluate an approximation to the rate constant, one will still need to compute $W^{\text{QC}}(T, z)$

for z equal to z_* and to the value z_R that corresponds to the reactant window (or bin), but this requires only two calculations of the averaged quantities needed for evaluating $\Delta W_{\text{vib}}(T, z)$. All the following equations are valid for either choice of z_* . In principle, the quasiclassical optimization of z_* should yield more accurate rate constants than the classical optimization, but the dominant error in the latter may be removed by the transmission coefficient of stage 2 or 3 so that the choice of optimization procedure will be less critical if one proceeds to stage 2 or 3 than if one stops at stage 1.

In stage 1, the transmission coefficient is taken as unity. Then the classical mechanical rate constant is

$$k^{\text{CM}}(T) = \frac{k_B T}{h} \exp[-\beta \Delta G_{\text{act}, T}^{\text{CM}}(z_*)] \quad (4)$$

and the quasiclassical rate constant based on the single reaction coordinate (SRC) z of stage 1 is

$$k^{\text{QC-SRC}}(T) = \frac{k_B T}{h} \exp[-\beta \Delta G_{\text{act}, T}^{\text{QC-SRC}}(z_*)] \quad (5)$$

where k_B is Boltzmann's constant, h is Planck's constant, β is $1/RT$, and $\Delta G_{\text{act}, T}^{\text{QC-SRC}}(z_*)$ is the free energy of activation for temperature T with the generalized transition state defined by $z = z_*$. Note that $\Delta G_{\text{act}, T}(z)$ has no dependence on a standard-state concentration because we are considering a unimolecular reaction of the substrate already bound to the enzyme. (One could extend the present formulation to bimolecular reactions straightforwardly, but we will give formulas only for the unimolecular case because it simplifies the notation.) The free energies of activation are given by

$$\Delta G_{\text{act}, T}^{\text{CM}}(z) = W^{\text{CM}}(T, z) - [W^{\text{CM}}(T, z_R) + G_{R, T, F}^{\text{CM}}] + C(T, z) \quad (6)$$

and

$$\Delta G_{\text{act}, T}^{\text{QC-SRC}}(z) = W^{\text{QC}}(T, z) - [W^{\text{QC}}(T, z_R) + G_{R, T, F}^{\text{QC}}] + C(T, z) \quad (7)$$

where $G_{R, T, F}^{\text{CM}}$ is the additional classical mechanical vibrational free energy of the reactant that must be added to $W^{\text{CM}}(T, z_R)$ to account for the mode, F, that correlates with the progress coordinate z (note that mode F is normal to the generalized transition state and is missing in $W(T, z)$), and $G_{R, T, F}^{\text{QC}}$ is the quantized value of this quantity. The correction term $C(T, z)$ comes from the Jacobian of the transformation^{42,48,49} from a locally rectilinear reaction coordinate, as assumed in derivations of the conventional transition state theory rate expression,^{71,76} to the curvilinear reaction coordinate z . (Note that z is curvilinear because the right-hand side of eq 1 is a nonlinear function of Cartesian coordinates.) Previous experience shows that $C(T, z)$ is small,^{42,48,90} and we will neglect it.

To calculate $G_{R, T, F}^{\text{CM}}$ for use in eq 6, we need to estimate the difference between the classical mechanical free energy of the reactants with and without the z coordinate. This is done by carrying out the calculation of vibrational frequencies at z_R , first with the reaction coordinate projected out and then without projecting out the reaction coordinate. The difference (in the approximation of effective harmonic modes) between the classical mechanical vibrational free energy of the $3N_1 - 6$ highest-vibrational-frequency modes of the latter calculation and the classical mechanical vibrational free energy of the $3N_1 - 7$ highest-vibrational-frequency modes of the former is

$$G_{R, T, F}^{\text{CM}} = -RT \left[\sum_{m=1}^{3N_1-6} \ln(k_B T / \hbar \omega_m^{\text{NP}}) \right] + RT \left[\sum_{m=1}^{3N_1-7} \ln(k_B T / \hbar \omega_m^{\text{P}}) \right] \quad (8)$$

where ω_m^{P} and ω_m^{NP} denote the average vibrational frequencies with and without projection. Note that these frequencies depend on the masses. The calculation of $W^{\text{QC}}(T, z_R) + G_{R, T, F}^{\text{QC}}$ for eq 7 is carried out by the following formula:

$$W^{\text{QC}}(T, z_R) + G_{R, T, F}^{\text{QC}} = W^{\text{CM}}(T, z_R) + G_{R, T, F}^{\text{CM}} + \Delta W_{\text{vib}, R}(T) \quad (9)$$

where $\Delta W_{\text{vib}, R}(T)$ is calculated like $\Delta W_{\text{vib}}(T, z)$, except that no projection operator is applied to remove the reaction coordinate, and we retain the $3N_1 - 6$ highest vibrational frequencies for the calculation of $\Delta W_{\text{vib}, R}(T)$, as compared to keeping the $3N_1 - 7$ highest vibrational frequencies for the calculation of $\Delta W_{\text{vib}}(T, z)$. Note that the last two terms in eq 9 depend on the masses, and hence, the left side of eq 9 also depends on the masses.

Stage-2 calculations are carried out using an equilibrium distribution of secondary-zone configurations in the bin corresponding to $z = z_*$, where z_* is the location of the stage-1 variational transition state (as optimized in step 1 or step 2 of stage 1). For each transition state configuration, $i = 1, 2, \dots, I$, we freeze the secondary-zone atoms and optimize the saddle point structures of the primary-zone atoms by treating them as a cluster embedded in the potential field of the fixed secondary-zone atoms. Then we calculate an isoinertial minimum-energy path (MEP) through the $3N_1$ -dimensional primary zone by the embedded cluster method.^{21,22,75,87} (An isoinertial MEP^{100,101} is the path of steepest descents through an isoinertial coordinate system. An isoinertial coordinate system is also called a mass-weighted or mass-scaled coordinate system, and an isoinertial MEP is also called an intrinsic¹⁰² reaction path.) The signed distance (through the isoinertial coordinate system, scaled^{64,74} to a reduced mass of 1 amu) from the saddle point along this MEP is called s , which is the reaction coordinate. The MEP terminates for negative s at R and for positive s at P, where R and P denote the reactant and product complexes of the unimolecular chemical step of the enzyme-catalyzed reaction, although in practice the calculated transmission coefficient often converges without having to extend the MEP all the way to R and P. It is useful to have systematic names for two additional points along the MEP. The point for which z equals $z_{*,i}$ (the precise value of z_* from the $z = z_*$ bin for secondary-zone configuration i) is labeled $s_{0,i}$. The stage-2 canonical variational transition state location (see next paragraph) for secondary-zone configuration i is called $s_{*,i}^{(2)}$.

Whereas stage 1 is based on a single reaction coordinate, in stage 2, we introduce a new reaction coordinate for each secondary-zone configuration i . Formally, when we average the transmission coefficient over i , this is equivalent to letting the secondary zone participate in the reaction coordinate; however, the present formalism provides a way of including this kind of physical effect implicitly, without requiring one to explicitly define such a coupled reaction coordinate. (The stage 2 reaction coordinates are also used, without change, in stage 3.)

For configuration i , the stage-2 embedded-cluster calculation yields a generalized transition-state free energy of activation $\Delta G_{T,i}^{\text{GT}}(s)$ and a semiclassical transmission coefficient $\kappa_i^{(2)}(T)$ by employing methods fully described in previous work.^{45,59,71-89} (In particular, $\Delta G_{T,i}^{\text{GT}}(s)$ is defined like the quantity called $\Delta G^{\text{GT}}(T, s)$ in ref 72, and $\kappa_i^{(2)}$ is defined analogously to $\kappa^{\text{CVT/VAG}}$

in ref 72). In a canonical ensemble of primary systems interacting with this frozen secondary-zone configuration, the minimum-flux dividing hypersurface is the one with maximum $\Delta G_{T,i}^{\text{GT}}(s)$, which is located at $s = s_{*,i}^{(2)}$ (this defines $s_{*,i}^{(2)}$), and the equilibrium classical flux is reduced relative to the dividing hypersurface that corresponds to $z = z_*$ by a factor⁷²

$$\Gamma_i^{(2)} = \exp\{-\beta[\Delta G_{T,i}^{\text{GT}}(s_{*,i}^{(2)}) - \Delta G_{T,i}^{\text{GT}}(s_{0,i})]\} \quad (10)$$

Equation 10 may be called the quasiclassical transmission factor. The quasiclassical rate constant at stage 2 is

$$k^{\text{QC-SSZ}}(T) = \langle \Gamma^{(2)} \rangle k^{\text{QC-SRC}}(T, z_*) \quad (11)$$

where

$$\langle f \rangle \equiv \Gamma^{-1} \sum_{i=1}^I f_i \quad (12)$$

for any function f that depends on the secondary-zone configuration i .

The net effect of quantum effects on the reaction coordinate motion, relative to rate constant reduced by eq 10,⁷² is given by proper inclusion of the semiclassical transmission coefficient $\kappa_i^{(2)}$. This net effect results from tunneling at energies below the effective barrier and from nonclassical diffractive reflection from the barrier top at energies above the effective barrier. The net effect is usually to increase the reactive flux because the tunneling has a larger Boltzmann weight than does the nonclassical reflection. Although $\kappa_i^{(2)}$ (and $\kappa_i^{(3)}$ below) includes both tunneling and nonclassical reflection, we follow the usual convention of just mentioning the tunneling aspect most of the time when we discuss it.

Putting the classical recrossing factor and tunneling effects together gives a stage-2 net transmission coefficient of

$$\gamma_i^{(2)} = \kappa_i^{(2)} \Gamma_i^{(2)} \quad (13)$$

Averaging the transmission coefficients over I secondary-zone configurations gives the final stage-2 rate constant:

$$k^{\text{CVT/MT-SSZ}}(T) = \langle \gamma^{(2)} \rangle k^{\text{QC-SRC}}(T, z_*) \quad (14)$$

where MT denotes multidimensional tunneling and may be SCT, LCT, or μ OMT. Note that recrossing of the stage-1 transition-state hypersurface and tunneling are not separable effects, i.e., $\langle \Gamma^{(2)} \kappa^{(2)} \rangle \neq \langle \Gamma^{(2)} \rangle \langle \kappa^{(2)} \rangle$.

Note that $k^{\text{CVT/MT-SSZ}}(T)$ contains the full reactant partition function based on the molecular dynamics calculations augmented by the quantized vibrational energy estimate; this reactant partition function includes, in principle, multiple conformational states of the secondary zone and the effect of primary zone–secondary zone coupling, as well as modes of vibration and libration that are localized in the primary zone. This is an improvement over the method employed in refs 21 and 22, where the reactant partition function for each configuration i was based on averaging over several results, each of which corresponds to a single local minimum of the potential energy of the primary zone in a single-secondary-zone configuration.

In stage 2, the thermal energy and entropy of the secondary-zone atoms are included through $k^{\text{QC}}(T, z_*)$ but not in the transmission coefficient. These contributions are incorporated in the transmission coefficient in stage 3. In stage 3, for each

secondary-zone configuration i , we freeze the primary-zone atoms along the reaction path of stage 2 at a sequence of N_s structures approximately evenly spaced along s , and for each of these, we equilibrate the secondary-zone subsystem (to be called the bath) by simulations in their presence to calculate the relative bath free energy as a function of s . The difference in bath free energy for two points on the reaction path is carried out employing free energy perturbation theory.^{103–105} The N_s structures on the reaction path include the saddle point (denoted S, with $s = 0$). The bath free energies $G_{\text{bath},i}(s)$ obtained in this stage are relative free energies, and only differences of the form $G_{\text{bath},i}(s) - G_{\text{bath},i}(s')$ are meaningful; calculated observables (such as rate constants) are independent of the zero of energy of the $G_{\text{bath},i}(s)$ scale. Note that the bath includes not only solvent but also all other atoms in the secondary zone, most or all of which may be protein atoms. Computational details of the calculation of $G_{\text{bath}}(s)$ are given in section 4; the present section focuses on more general aspects of the method. Note also that $G_{\text{bath}}(s)$ also depends on T but for simplicity we suppress this in the notation.

The stage-3 effective potential of mean force on reaction path i is

$$W_i^{(3)}(T, s) = \Delta G_{T,i}^{\text{GT}}(s) + G_{\text{bath},i}(s) - G_{\text{bath},i}(s = 0) \quad (15)$$

where the last term sets an arbitrary but convenient normalization for the free energy scale. This leads to an improved estimate of the quasiclassical transmission factor, which is now given by

$$\Gamma_i^{(3)} = \exp\{-\beta[W_i^{(3)}(T, s_{*,i}^{(3)}) - W_i^{(3)}(T, s_{0,i})]\} \quad (16)$$

where $s_{*,i}^{(3)}$ is the value of s where $W_i^{(3)}(T, s)$ is a maximum.

The small-curvature tunneling factor is then evaluated by using $W_i^{(3)}(T, s)$ as the zero-order canonical mean-shape potential⁴⁵ and taking the reaction-path curvature from stage 2. The large-curvature tunneling calculation requires that $W^{(3)}(T, s)$ also be interpolated off the MEP, which involves additional approximations. Interpolations required for stage-3 calculations were carried out by the VTST-ISPE- $(N_s - 3)$ algorithm.^{106,107} The resulting semiclassical transmission coefficient is called $\kappa_i^{(3)}$.

The quasiclassical transmission coefficient for stage 3 is $\langle \Gamma^{(3)} \rangle$, and the quasiclassical rate constant is

$$k^{\text{QC-ESZ}}(T) = \langle \Gamma^{(3)} \rangle k^{\text{QC-SRC}}(T, z_*) \quad (17)$$

The overall transmission coefficient for stage 3 for bath configuration i is

$$\gamma_i^{(3)} = \kappa_i^{(3)} \Gamma_i^{(3)} \quad (18)$$

and the rate constant including tunneling is

$$k^{\text{CVT/MT-ESZ}}(T) = \langle \gamma^{(3)} \rangle k^{\text{QC-SRC}}(T, z_*) \quad (19)$$

Stages 2 and 3 yield improved approximations to the rate constant by providing a semiclassical CVT extension of the classical dynamical method of Keck,⁶⁰ Anderson,⁶¹ and Bennett,³⁶ which was extended to enzyme reactions by Neria and Karplus.⁶⁶ Because we use CVT rather than full dynamics, we neglect the recrossing of the $s = s_{*,i}$ transition state because, although the quasiclassical transmission coefficient accounts for some of the recrossing of the $s = s_{0,i}$ transition state, it does not account for classical recrossings of the stage-2 or stage-3 variational transition state at $s_{*,i}$. A procedure (the unified

dynamical method) for combining classical recrossing corrections at the best transition state with semiclassical transmission coefficients is presented elsewhere,^{64,65} but is not employed here. (Estimating the recrossing on the basis of classical trajectories need not improve the accuracy because the trajectories do not properly enforce the quantum mechanical character of vibrational motions.)

As mentioned above, the method including stage 3 will be called the equilibrium secondary zone (ESZ) approximation. The present three-stage ESZ algorithm for the transmission coefficient is an improvement over the separable equilibrium solvation (SES) approximation^{88,89} for reactions of small molecules in liquids. In that approximation, one optimizes the geometry of reactants, products, and saddle point in the gas phase and calculates gas-phase minimum-energy paths and tunneling paths. Then, when one calculates rate constants, one adds equilibrium free energies of solvation to the gas-phase energies at these structures and along these paths. In principle, the present method is the same except that the solute is replaced by the primary subsystem, the solvent is replaced by the secondary zone (also called the bath), gas-phase calculations on the solute are replaced by calculations on the primary-zone atoms in the presence of typical configurations of the secondary-zone atoms, and the solvation free energy is replaced by the bath free energy. Furthermore, whereas the SES method is used to calculate the free energy of activation and the transmission coefficient, the ESP approximation is used to calculate an ensemble-averaged transmission coefficient for a free energy of activation calculation in which the secondary zone is classically fully coupled to the primary zone. In practice, there is another difference. In small-molecule SES calculations, the solvation free energy is calculated directly every time it is needed. In the practical scheme suggested here (which is not an intrinsic part of the physical approximation), the bath free energy is calculated at only about 10 points (we actually use $N_s = 5$ in the present paper) and is interpolated to all other geometries where it is needed by the VTST-ISPE^{106,107} algorithm.

We can also compare the present three-stage ESZ approximation to the two-stage approximation, i.e., the SSZ method. Neither approximation assumes that the secondary zone is separable because in both cases the reaction path (which includes the saddle point structure and reactant and product structures) is determined in the presence of the secondary zone. In both cases, the reaction path is determined in the presence of a typical configuration of the secondary zone.

In the SSZ approximation, the secondary-zone atoms provide an external potential along the path, whereas in the ESZ approximation, they are fully equilibrated to the path. However, unlike the equilibrium solvation path^{88,89} (ESP) approximation for reactions of small molecules in liquids, the ESZ reaction path is not self-consistent with its surroundings. One could imagine an equilibrium secondary-zone approximation, in which the reaction path is determined as the path of steepest descent on an energy surface consisting of the potential energy of the primary zone and free energy of the secondary zone (rather than the path used here which is based on the potential energy for both zones), but this would be prohibitively expensive for large systems. (It is not clear which method would be more accurate.) Note that the ESZ reaction path is only used for computing the stage-3 transmission coefficient, and thus, it is only necessary to determine it accurately in the vicinity of the variational transition state.

Additional Comments on Notation. The notation one uses depends on what one is emphasizing. In the development above,

we emphasized the relation to one another of the results obtained in successive stages and steps of those stages, and we also emphasized the physical nature of the assumptions underlying the various transmission coefficients. However, in discussing the resulting rate constants in a broader context, one may wish to emphasize the use of variational transition state theory (VTST), in particular the canonical variational theory (CVT). We use the label CVT to denote any calculation that maximizes a free energy of activation or minimizes the flux through a generalized transition state hypersurface for a thermal ensemble, independent of whether one uses fixed-volume, fixed-pressure, or stochastic boundary conditions. Then the CM results or any of the QC results could be labeled VTST or CVT, just as the stage-2 and stage-3 results that include tunneling effects were labeled CVT/MT.

In the present work, we use CVT in stage 1, which can in principle be carried out with considerable freedom in the choice of reaction coordinate. In stage 2 or stages 2 and 3, we employ an ensemble of transition states from stage 1 and a minimum-energy reaction path through the primary zone that depends on the stage-1 coordinates of the secondary zone, and we compute the transmission coefficient by ensemble-averaged variational transition state theory with multidimensional tunneling (EA-VTST/MT).

3. System

3.1. Experimental Background. LADH is a metalloenzyme containing two Zn atoms, one of which plays a structural role and the other of which plays a catalytic role with the initial alcoholic oxygen and the final aldehyde oxygen participating in its 4-fold coordination shell. The reaction mechanism involves an initial proton-transfer step from the alcoholic substrate into a hydrogen-bonding network, in a preequilibrium favoring the anion.^{3,108–111} Thus, the chemical step is assumed to be a hydride transfer from C-1 of the alcoholate to C-4 of NAD⁺, which is the main focus of the present study. Although the rate of ethanol dehydrogenation in wild-type LADH is limited by release of the product,^{111–113} the chemical step may be “unmasked” in the kinetics by changing the substrate to benzyl alcohol or para-substituted benzyl alcohols and by mutagenesis at hydrophobic residues surrounding the active-site binding pocket.⁴ The overall picture that emerges from a series of studies by Klinman and co-workers is that the chemical step in alcohol dehydrogenation by wild-type LADH, mutant LADH, and yeast alcohol dehydrogenase all involve significant amounts of tunneling,⁶ but this is sometimes masked by kinetic complexity. Observed primary kinetic isotope effects (KIEs) for the hydride transfer step in various alcohol dehydrogenase transformations of benzyl alcohol and para-substituted benzyl alcohols are $k_H/k_D = 3.7–4.7$ and $k_H/k_T = 7.0–7.8$, and observed secondary kinetic isotope effects at the C-1 position of the alcohol are $k_H/k_D = 1.2–1.3$ and $k_H/k_T = 1.3–1.4$.^{2–4,7} Klinman and co-workers inferred significant tunneling contributions to the process primarily from two observations: (1) The Swain–Schaad¹¹⁴ exponent α , defined by

$$\alpha = \ln(k_H/k_T)/\ln(k_D/k_T) \quad (20)$$

is in the range 4–10,^{2–5,7} whereas values greater than 3.34 are sometimes assumed (on the basis of transition state theory arguments) to be an upper limit in the absence of tunneling.¹¹⁵ (2) The ratio of Arrhenius pre-exponential factors A_H/A_T for the primary KIE sometimes has a value as low as 0.5,⁵ whereas a value below 0.6 is sometimes considered a lower limit in the absence of tunneling.¹¹⁶

In the present work, we study the chemical step (unimolecular conversion of the ternary alcohol complex to the ternary aldehyde complex) of wild-type LADH reaction with unsubstituted benzyl alcohol. In particular, we have chosen the horse liver alcohol dehydrogenase, whose crystal structure is available for the ternary complex with 4-bromobenzyl alcohol and NAD^+ (2.9 Å)¹¹⁷ and for the ternary complex with 2,3,4,5,6-pentafluorobenzyl alcohol and NAD^+ (2.1 Å)¹¹⁸ and whose kinetics were studied by Klinman and co-workers.⁴ The overall kinetics and thermodynamics of the chemical step have been thoroughly analyzed for this case, leading to the conclusion that the overall free energy $\Delta G_{\text{act},303^\circ}$ is +1 kcal/mol, and the phenomenological free energy of activation $\Delta G_{\text{act},303^\circ}$ is 15.6 kcal/mol.^{111,112} Although experimental enthalpy changes are unavailable for LADH, it is noteworthy that $\Delta H_{\text{act},298^\circ}$ for yeast alcohol dehydrogenase is 8 kcal/mol less than $\Delta G_{\text{act},298^\circ}$ because of a large negative entropy of activation.³ The negative entropy of activation may be associated with loss in the number of accessible conformations.¹¹⁹ We note that the hydride transfer step is not rate-limiting in the wild-type enzyme. The experimental rate constant for each individual mechanistic step was obtained by fitting kinetic equations to the observed reaction rate.

3.2. Potential Energy Function. The potential energy function was created by a combined quantum mechanical/molecular mechanical/valence bond (QM/MM/VB) method. A subset of the terms correspond to a standard QM/MM method,^{120–123} and in particular, we use the generalized hybrid orbital (GHO) method¹²³ to treat the QM-MM boundary. In this method, the system is divided into an N_{QM} -atom QM part (denoted by “QM”) and an N_{MM} -atom MM part (denoted by “MM”). The total number of atoms is $N = N_{\text{QM}} + N_{\text{MM}}$. The QM part is joined to the MM part at N_{B} single bonds; the QM atoms involved in these bonds are called boundary atoms, and these boundary atoms are actually treated by a combination of QM and MM terms as explained elsewhere.¹²³

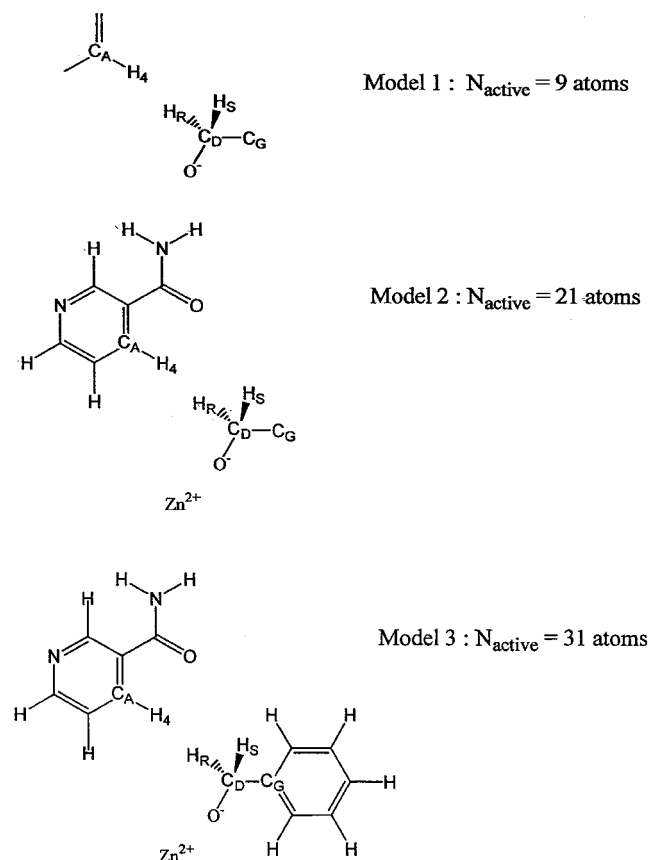
For the present application, the retained part of the protein has 260 residues (coming from both units of the dimer), N is 5560, N_{QM} is 54, N_{MM} is 5506, and N_{B} is 4. The QM part of the system, which has a net zero charge, is taken to include the catalytic Zn, the side chain of the ligated histidine up to its C_α atom, which is taken as a boundary atom (12 atoms), the side chains of the two ligated cysteines up to their C_α atoms, which are taken as boundary atoms (5 atoms each for a total of 10), the nicotinamide portion of NAD^+ including the 1'-carbon atom of ribose, which is taken as a boundary atom (16 atoms), and the entire benzyl alcoholate substrate (15 atoms). See Scheme 1. The molecular mechanics atoms consist of the structural Zn, 3849 other protein atoms, the 54 remaining atoms of the coenzyme, and 1602 atoms from 534 water molecules.

The QM part, including the boundary atoms, is represented by the semiempirical AM1 model, which treats the valence electronic structure explicitly. The total potential energy surface for the entire N -atom system is given as follows:

$$V = \langle \Psi | H_{\text{QM}} + H_{\text{QM,MM}}^{\text{elec}} | \Psi \rangle + E_{\text{aux}} + V_{\text{MM}} + V_{\text{QM,MM}}^{\text{vdW}} + V_{\text{SEVB}} \quad (21)$$

The first four terms on the right-hand side of eq 21 are the same as those in the original¹²³ GHO calculations, and the final term (V_{SEVB}) is new in ref 22. In eq 21, ψ is the quantum mechanical wave function of the QM valence subsystem, H_{QM} is the quantal Austin-Model-1 Hamiltonian^{124–126} of the QM subsystem (including valence–valence, valence–core, and core–core

SCHEME 1: Schematic Representation of the Quantum Mechanical Region and Boundary Atoms in the Liver Alcohol Dehydrogenase System for $N_1 = 9, 21$, and 31



terms), $H_{\text{QM/MM}}^{\text{elec}}$ contains the Coulomb interaction between the electrons and cores of the QM system and the partial atomic charges of the MM system, E_{aux} is the energy associated with the auxiliary orbitals of the GHO scheme, $V_{\text{QM,MM}}^{\text{vdW}}$ represents the van der Waals interactions of all QM atoms with the MM subsystem, V_{MM} is the sum of the van der Waals and Coulomb interactions between MM atoms, plus the stretching, bending, and torsional terms, and V_{SEVB} is a semiempirical valence bond term^{127–130} that depends only on coordinates in the QM system. The MM parameters are taken from the CHARMM-22^{131–133} and TIP3P¹³⁴ models. The V_{SEVB} is used to sculpt the finer details of the potential energy surface in order to provide a better molecular model of the system of interest.

Full details of the potential are provided in our previous paper.²²

4. Details of Dynamics Calculations

The calculations in the ensembles were carried out with $T = 298$ K by stochastic boundary molecular dynamics,^{135–137} and with most details as in our previous papers.^{21,22} In particular, the reactant is assumed to be benzyl alcoholate anion, which is formed prior to the chemical step (the proton is assumed to be transferred to His-51). The reaction region, which is centered at the midpoint between the acceptor and donor carbons, has a radius of 20 Å, and it is surrounded by a buffer region of shell thickness 4 Å, consisting of all water and amino acid residues that have any atoms within 24 Å from the midpoint between the acceptor and donor carbons. Other atoms are omitted in the stochastic boundary molecular dynamics calculation.^{135–137} The classical part of the reactant region is treated by unconstrained Hamiltonian dynamics and the buffer region by constrained

Langevin dynamics. The secondary zone includes the entire buffer plus that part of the reactant region which is not part of the primary system. The runs were started from the X-ray structure of Ramaswamy et al.¹¹⁸ The benzyl alcoholate is unprotonated, and His-51 is protonated, in accord with the proton relay mechanism of Ramaswamy et al.¹¹⁸

First we performed a classical mechanical molecular dynamics simulation of the reactants to equilibrate the system. Then we performed umbrella sampling over a series of windows centered at

$$z_k = z_R + (k - 1)\Delta z_k \quad (22)$$

where $k = 1, 2, \dots, N_z$ and Δz_k represents the width (0.1–0.4 Å) of a simulation window. We found that N_z equal to 11 was sufficient to reach products. Analyzing the results from these calculations yielded $W^{\text{CM}}(T, z)$. Each run includes 20 ps of equilibration and 50 ps of ensemble averaging. In the present study, as in our previous two papers,^{21,22} we select configurations according to $W^{\text{CM}}(T, z)$ using pure classical mechanics.

The primary-system geometry optimizations and reaction-path calculations were carried out by interfacing the POLYRATE dynamics program to the CHARMM energy and gradient routines. Geometry optimization of the primary-zone reactant and product species were performed using the BFGS method, while saddle-point geometry was obtained using the Newton–Raphson method with Brent line minimization at a gradient convergence of 10^{-7} atomic units.^{69b} The reaction path was traced using the Euler steepest descent method in mass-weighted coordinates with a step size of 0.002 bohr. The Hessian along the reaction path was determined numerically by a central difference scheme and a step size of 0.01 bohr, and the generalized normal modes were calculated in rectilinear coordinates. In the present paper, we did not include quantum mechanical vibrational energy in optimizing z_* , but it could be done, and for some reactions, it will be very important to do so.

The stage-2 results were calculated with $N_1 = 21$. The primary zone is shown in Scheme 1. The 21 active atoms consist of C–CH₂O from the alcoholate, the Zn, and NAD excluding the 1' sugar carbon and beyond. The stage-2 results were averaged over 18 secondary-zone configurations ($I = 18$). In particular, the averages appearing in eqs 11 and 14 were calculated from a subset of 18 configurations corresponding to the stage-1 window with the highest $W^{\text{CM}}(z)$. It would be appropriate to take these from the highest free energy bin of the umbrella sampling calculation, but in the present paper, they were generated in a separate 50 ps run with restraints for computational convenience. These 18 configurations were also used for calculating $\Delta W_{\text{vib}}(T, z_*)$ in eq 3, and 18 configurations from the reactant window were used to compute the frequencies for eq 8 and to compute $\Delta W_{\text{vib},R}(T)$ in eq 9. These 18 transition state configurations and 18 reactant configurations give a sparse but representative sample of the fluctuation of the bath. The values of $W^{\text{CM}}(T, z_*)$ and $W^{\text{CM}}(T, z_R)$, in contrast, are based on much larger numbers of configurations, using umbrella sampling.

For stage 3, we selected two of the 18 transition state configurations used for $z = z_*$ in stage 2. These two configurations were typical ones in that the stage-2 results averaged over these two configurations are very similar to those averaged over all 18 (see below).

For the semiclassical calculations, the free energy of activation was calculated using the reorientation of the dividing hypersurface^{140,141} (RODS) algorithm. The small-curvature tunneling calculations were carried out using the centrifugal-dominant small-curvature semiclassical adiabatic algorithm,⁷⁹ and the

large-curvature tunneling calculations were carried out using the version 4⁸⁰ algorithm.

The relative bath free energies of stage 3 are calculated by free energy perturbation theory,^{103–105,138,139} in the present study, we used the method of ref 105. We took $N_z = 11$ and $\Delta z_k = 0.1$ –0.4 Å in stage 1, as mentioned above. In stage 3, we use $N_s = 5$ with windows at $s = -1.06, -0.53, 0, +0.53$, and $+1.06$ Å. We again used z as the independent variable for umbrella sampling, and we converted s to z and $G_{\text{bath}}(z)$ to $G_{\text{bath}}(s)$ by locally fitting $z(s)$ along the reaction path of stage 2.

For each of the stage-3 windows, we ran a minimum of 40 ps to heat and equilibrate the system and then 30 ps of data collection. The bath contribution to the free energy was calculated by including only the solute–solvent and solvent–solvent terms in the perturbing Hamiltonian. The double-wide sampling scheme¹⁰³ was employed in which a sample at $s = s_0$ is used to evaluate the perturbation at $s = s_0 \pm 0.5\Delta s$, where Δs is the distance between windows. Thus, $0.5\Delta s$ is 0.265 Å, and the perturbation is acceptably small.

For kinetic isotope effect calculations, we used the same typical configurations for all isotopic versions of the reaction. These were obtained in classical simulations in which all hydrogens are protium.

The details of the CVT/ μ OMT calculations for stage 3 were the same as for stage 2 except that $W_i^{(3)}(T, s)$ replaces $G_{T,i}^{\text{GT}}(s)$.

5. Results and Discussion

5.1. Reaction Profile. Figure 1A depicts the average QM electronic-nuclear energy of primary-zone atoms and the computed potential of mean force (PMF) along the reaction path z . The average QM energy change from the reactant benzyl alcoholate to the product benzaldehyde is -14 kcal/mol. This may be compared with a heat of reaction of about -50 kcal/mol for the hydride transfer from benzyl alcoholate to NAD⁺ in the gas phase. The QM energy shown in Figure 1A contains the effect of coordination of the substrate to the Zn²⁺ ion in the active site, which dramatically reduces this energy change. Inclusion of interactions with the enzyme-solvent environment and protein dynamic fluctuations increases the activation energy and decreases the exothermicity and exoergicity of the reaction. This is illustrated by the PMF for the hydride transfer reaction catalyzed by LADH, which is also shown in Figure 1A as a function of the reaction coordinate z . Since the computed PMF in Figure 1A is the result of a delicate balance of the intrinsic reactivity of the “QM” substrate-coenzyme system and its interactions with the metal ion and the rest of the protein, it is important to carry out free energy calculations to estimate the activation barrier, as opposed to performing energy minimization only or performing energy minimization first, followed by free energy perturbation along this fixed reaction path.

The computed classical mechanical free energy of activation for the hydride-transfer step of the enzymatic reaction is $\Delta G_{\text{act},T}^{\text{CM}}(z_*)$, where z_* denotes the maximum of this classical quantity, and we obtain a value of 15.3 kcal/mol for this quantity. After the second step of stage 1, the computed free energy of activation is $\Delta G_{\text{act},T}^{\text{QC}}(z_*)$, for which we obtain a value of 13.7 kcal/mol, including quantum mechanical vibrational free energies. For comparison, the experimental phenomenological free energy of activation is 15.6 kcal/mol.^{111,112} At this point in our calculation, we have assumed that the classical dynamic transmission coefficient is unity, although the shape of the transition state hypersurface is as not as physical as when defining it using a minimum-energy path, and so there is probably some recrossing. For example, a value of 0.43 has

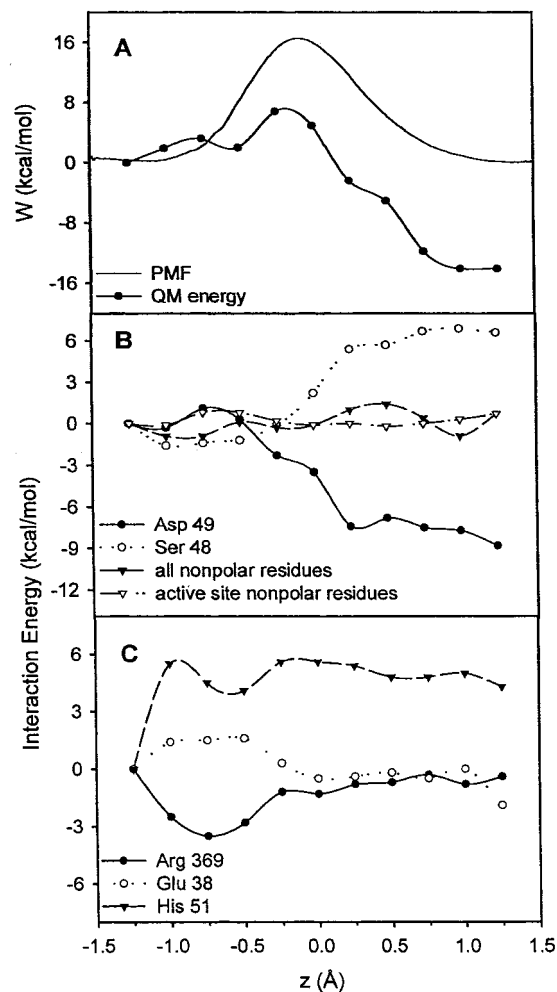


Figure 1. (A) $W^{CM}(T,z) - W^{CM}(T,z_R)$ (plain solid curve) and sum of the first two terms and fifth term in eq 19 relative to the reactants (solid curve with heavy dots added). (B, C) Electrostatic interaction energies, relative to their values for the reactant complex, of all hydrophobic residues and those within 5 Å of the substrate and coenzyme and of individual polar residues within 5 Å of the substrate and coenzyme (nonligand residues) with the QM subsystems as functions of the reaction coordinate.

been estimated for this kind of hypersurface for the proton-transfer reaction in the active site of triosephosphate isomerase using the method of rare-event dynamics simulation.⁶⁶ A transmission coefficient of 0.43 would raise the calculated phenomenological free energy of activation by 0.5 kcal/mol. With or without this correction, the computed free energy of activation for the hydride transfer reaction by LADH is in reasonable accord with experiment, suggesting that the combined semiempirical AM1/CHARMM/SEVB potential is adequate for this reaction and it can be used to derive kinetic isotope effects in the enzymatic process.

From the values in the previous paragraph, we see that quantizing vibration while continuing to base the calculation on a single reaction coordinate lowers the calculated effective barrier height by 1.6 kcal/mol. The result is comparable to that found by our earlier method.²² Billeter et al.³² included the hydrogen quantal vibrational effects in the free energy profiles of their own hybrid approach and also found that such effects decrease the free energy barrier: In their case, the effect is computed to be 1.8 kcal/mol. Since they used a different potential energy function than the one used here and quantized only three degrees of freedom (as compared to 56 here for

generalized transition states and 57 here for reactants), the precise agreement to within 0.2 kcal/mol is probably fortuitous, but the general agreement of the two approaches is encouraging.

The active site of LADH is characterized by hydrophobic and hydrogen bonding interactions with the NAD cofactor and the substrate. The backbone carbonyl groups of Val-292 and Ala-317 form hydrogen bonds with the amide group of nicotinamide, while the backbone amide group of Phe-319 donates a hydrogen bond to the nicotinamide carbonyl oxygen. These hydrogen-bonding interactions play an anchoring role in fixing the position of NAD^+ in the active site. Overall, a hydrophobic environment accommodates the pyridine ring on the opposite side of the substrate, where the hydride transfer reaction occurs. Dynamic motions of Val-203 (Figure 2a), which are coupled with fluctuations of the nicotinamide moiety, have been noted previously by Bruice and co-workers,^{142,143} and the ring was found to preferentially pucker toward the substrate. This leads to a conformation favorable for the hydride transfer step in LADH. The phenyl group of the substrate is also surrounded by hydrophobic residues (Figure 2a), including Leu-57, Phe-93, Leu-116, Leu-141, Val-294 and Ile-318. These predominantly van der Waals interactions, which make important contributions to substrate and NAD^+ binding, restrict the dynamic motions of the substrate and coenzyme and, consequently, affect the transition state region of the hydride transfer potential energy surface.

There is also a delicate hydrogen-bonding network in the active site of LADH, involving the benzyl alcoholate substrate, Ser-48, His-51, and the ribose hydroxyl groups; see Figure 2b. The residue Ser-48 donates a hydrogen bond from its hydroxyl side chain to the benzylic oxygen, which is coordinated to the Zn^{2+} ion. In turn, Ser-48 accepts a hydrogen bond from the 2'-hydroxyl group of the ribose, which is hydrogen bonded to His-51. This hydrogen bonding network plays a key role in the initial proton-transfer step to yield the active form of the benzyl alcoholate substrate in the hydride transfer step, and it is maintained during the hydride transfer step.

To provide insight into the energetic environment for the hydride transfer reaction, we have computed the interaction energies between the substrate and key residues along the reaction path. Individual amino acid contributions to the energy change are depicted in panels B and C of Figure 1, which are averaged over configurations generated during the umbrella sampling simulation. In particular, hydrophobic residues, which play a critical role in positioning the coenzyme NAD^+ and substrate benzyl alcoholate in a reactive conformation, do not appreciably change the potential energy surface along the reaction path (Figure 1B, triangle curves). In contrast, Ser-48 interacts with the anionic alcoholate about 6 kcal/mol more strongly than with the neutral aldehyde, and thus, it makes a large differential contribution to the reaction profile. Interestingly, the interaction energy between Ser-48 and the QM atoms increases sharply as the hydride transfer reaches the transition state, which is consistent with the charge-transfer event in the chemical step. This is in turn mirrored by a stabilizing effect from Asp-49, which is hydrogen-bonded to His-67, an active site Zn ligand. The removal of a negative charge from benzyl alcoholate reduces electrostatic repulsions with Asp-49. Consequently, Asp-49 introduces a net stabilization of the transition state and product state by 7–8 kcal/mol. Ionic residues that are within 7 Å of the primary hydrogen atom of the substrate have also been examined, and their energy contributions are shown in Figure 1C. Surprisingly, Arg-369 and Glu-68 do not

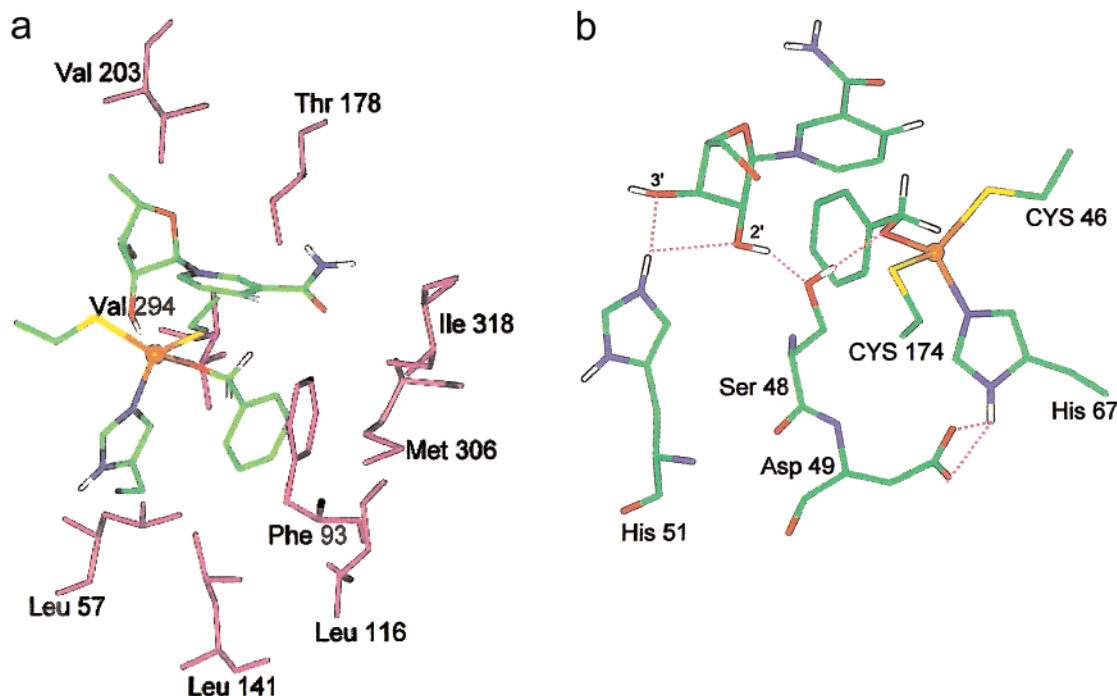


Figure 2. (a) Selected residues that form the hydrophobic binding pocket in the active site of liver alcohol dehydrogenase. (b) Hydrogen bonding network associated with the initial proton-transfer step from benzyl alcohol to His-51.

TABLE 1: Selected Average Interatomic Distances between Atoms of the Benzyl Alcoholate and Coenzyme at the Reactant and Transition State in the Active Site of Liver Alcohol Dehydrogenase^a

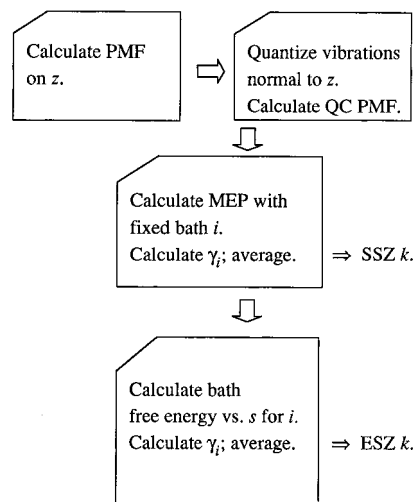
substrate or coenzyme	protein atom	reactant state	transition state
Hydrogen Bonding Interactions			
NAD-amide N	Val292 O	3.2	3.2
NAD-amide N	Ala317 O	3.3	3.3
NAD-amide O	Phe319 N	3.3	3.1
benzyl O	Ser48 O γ	2.7	2.8
rib-2' OH	Ser48 O γ	2.8	2.8
rib-2' OH	His51 Ne	3.6	3.2
rib-3' OH	His51 Ne	3.5	3.0
Hydrophobic Interactions			
NAD C4	Thr178 C γ	3.6	3.8
NAD C5	Thr178 C γ	4.3	4.2
NAD N1	Val203 C γ	4.4	4.5
NAD C6	Val203 C γ	3.7	3.9
NAD N1	Val294 C γ	4.0	3.9
NAD C2	Val294 C γ	3.6	3.7
benzyl C	Phe93 C ζ	3.6	3.8
benzyl C	Phe93 C δ	3.9	3.8
benzyl C	Leu116 C δ	3.9	4.7
benzyl C	Leu116 C γ	4.7	4.1
benzyl C	Leu141 C δ	5.0	5.1
benzyl C	Ile318 C δ	4.5	4.1

^a Distances are given in Ångströms, and the root-mean-square deviations are typically ± 0.3 Å.

significantly alter the potential energy surface for the hydride transfer in LADH, whereas His-51 destabilizes the QM atoms.

Table 1 lists the average distances between atoms of the substrate and NAD⁺ coenzyme and atoms of active site residues, which are obtained during the molecular dynamics simulation. The C γ atoms of Thr-178, Val-203, and Val-294 have close contacts with the nicotine amide ring, with average distances in the range of $3.6\text{--}4.4 \pm 0.3$ Å for both the reactant and transition state. Although there appear to be somewhat greater fluctuations in the transition state region, the average interaction distances are essentially the same in comparison with those at the reactant state. Residues within van der Waals contacts that

CHART 1: Flow Chart



are listed in Table 1 include Phe-93, Leu-116, and Leu-141. Table 1 also reveals that key hydrogen-bonding interactions in the active site are maintained during the hydride transfer process.

The C–H–C bond angle at the transferring hydride was analyzed all along the reaction path for one of the most typical solvent configurations. Along the minimum-energy path, this angle varies from 149° at the reactant Michaelis complex to 152° at the transition state.

5.2. Dynamics. The key steps in the dynamics algorithm are summarized in a flow chart (see Chart 1). A key component in our approach is to include quantum mechanical vibrational energy and tunneling corrections in the computation of rate constants and kinetic isotope effects for enzymatic reactions. Previously,²² we reported a two-stage approach, in which a set of stage-2 configurations are generated corresponding to the stage-1 transition state, and the rate constant, $k^{(2)}(T)$, is obtained by averaging over dynamic results from stage-2 configurations using VTST. There are two major improvements in the present

TABLE 2: Computed Potential Energy Differences, Free Energy of Activation, Free Energy of Reaction, and Imaginary Frequency at the Saddle Point for Three Models Containing 9, 21, and 31 Atoms, Respectively^a

	model 1	model 2	model 3
$V_i^{\text{SP}} - V_i^{\text{R}}$	7.7	13.3	13.8
$V_i^{\text{P}} - V_i^{\text{R}}$	0.8	2.9	0.7
$\Delta G_i^{\text{GT}} (s = 0)$	5.2	10.9	11.6
$G_i^{\text{P}} - G_i^{\text{R}}$	0.5	3.7	0.5
$\omega_i^\ddagger (\text{cm}^{-1})$	1036i	1058i	1061i

^a Energies are given in kcal/mol. R, SP, and P denote reactants, saddle point ($s = 0$), and product, respectively.

study. First, we implement an improved averaging scheme for calculating stage-2 rate constants. This involves introducing a transmission coefficient that accounts both for recrossing (through introduction of a transition state dividing hypersurface orthogonal to the primary-system isoinertial minimum-energy path rather than to the stage-1 transition state dividing hypersurface that is defined by constant z) and for tunneling (through introduction of multidimensional semiclassical tunneling contributions). Second, we further extend the previous algorithm by including stage-3 calculations that incorporate dynamic effects from the protein–solvent bath of stage-2 configurations.

In step 2 of stage 1 and in stages 2 and 3, the system is divided into a dynamic primary zone and a static secondary zone. Clearly, a major issue is the selection of atoms in the primary zone. In our paper on the enolase reaction,²¹ the entire region whose electronic energy was treated quantum mechanically was taken as the primary zone. However, for systems in which a greater number of atoms is treated quantum mechanically in the electronic structure step, it would be unnecessarily time-consuming to include all of them in the primary zone to determine the reaction path and the variational transition state. Thus, it is necessary to balance computational accuracy and efficiency in the selection process. To this end, we have examined three model systems that include, respectively, $N_1 = 9, 21$, and 31 atoms in the primary zone, which are depicted in Scheme 1. For each system, for stage 2, we froze the remainder of the system, i.e., the secondary zone (which is also called the bath), calculated the minimum-energy path of primary-zone atoms in mass-scaled coordinates (i.e., calculated the primary-system isoinertial MEP, also called the primary-system intrinsic reaction path), and calculated the transmission coefficient by CVT/ μ OMT using the embedded cluster model. The computed activation energies, free energy of reaction, and the imaginary vibrational frequencies, obtained in the semiclassical reaction path calculations for one of the 18 configurations used in the final averaging, are listed in Table 2. Clearly, the primary system of Model 1 is too small since the activation barrier is significantly underestimated. On the other hand, both model 2 and model 3 yield similar activation energies and the computed imaginary vibrational frequencies are also in good accord. In addition, the computed transmission coefficients are in good agreement between model 2 and model 3. Consequently, we decided to use model 2 in all subsequent calculations.

The small-curvature approximation was used for the μ OMT calculations on the basis of the variational criterion⁷⁸ that it yields larger tunneling probabilities than the large-curvature approximation at all energies. The thermally averaged LCG4 transmission coefficients are about 32% less than the SCT ones for the all-protium case and 19–24% less for other isotopic combinations.

The stage-2 transmission coefficient is averaged over 18 equilibrium configurations in the transition state, as discussed

TABLE 3: Average Transmission Coefficients for Static Secondary Zone (SSZ)^a

isotope ^a	$\langle \Gamma^{(2)} \rangle$	$\langle \kappa^{(2)} \rangle$		$\langle \gamma^{(2)} \rangle$	
		ZCT	μ OMT	ZCT	μ OMT
HH	0.983	1.68	2.495	1.64	2.42
HT	0.977	1.55	2.14	1.51	2.06
DD	0.976	1.74	2.352	1.69	2.27
DT	0.977	1.70	2.29	1.66	2.21
TH	0.977	1.71	2.40	1.67	2.34
TD	0.981	1.66	2.29	1.63	2.24

^a The first and second isotopes listed are the primary and secondary hydrogens, respectively. The same convention is also used in later tables.

in section 4. For each of these configurations, isoinertial minimum-energy paths are determined with various isotopic substitutions at the primary and secondary positions of the hydride transfer reaction in LADH. The computed average transmission coefficients for the six primary and secondary isotopic combinations of the benzyl alcoholate hydride transfer reaction in LADH are given in Table 3. An average value of $\kappa^{(2)} = 2.4$ is obtained for the hydride transfer from either the microcanonically optimized approximation or the small curvature-tunneling approximation, and this transmission coefficient represents a significant increase in rate constant due to quantum mechanical tunneling. Although this rate enhancement is only a small effect relative to the specific interactions in the enzyme that alter the rate by orders of magnitude, we shall see that it is essential to include it if one wants to obtain accurate kinetic isotope effects.

The fact that the ZCT method yields significantly smaller transmission coefficients than the μ OMT method (see Table 3) means that corner cutting is quantitatively important for tunneling in the LADH hydride transfer reaction. The variation in computed transmission coefficients for other isotopic substitutions is relatively small. Importantly, isotopic substitution at the secondary positions has greater influence on the computed transmission coefficients than primary isotope replacement. For example, there is only a 4% decrease in $\kappa^{(2)}$ in replacing the primary H by a T, whereas the decrease is 14% for the same type substitution at the secondary position. These trends will be reflected in the secondary KIE results that are presented below.

Although the frozen bath approximation in stage-2 calculation is reasonable for the short time scale of the barrier crossing, the dynamic contributions of the surrounding protein–solvent bath that affect the shape of the potential surface and the position of the transition state are excluded. These effects are now included in our stage-3 algorithm. Figure 3 shows the free energy change of the secondary-zone system along two reaction paths determined using the initial stage-2 configurations, and the computed average transmission coefficients in the ZCT and μ OMT approximations are given in Table 4.

Although we used 18 bath configurations for stage 2, which provides a good sample, we used only two bath configurations for stage 3, so these results have more statistical uncertainty. However, as illustrated in Table 5, the two configurations we chose for stage 3 are typical ones in that the stage-2 rate constants averaged over just these two configurations are in good agreement with those averaged over all 18 configurations. Thus, the difference observed here between stage-2 and stage-3 rate constants should be representative of a larger sample.

Computed rate constants for the hydride transfer in LADH along with various primary and secondary isotopic combinations are summarized in Table 5, which shows progressive changes

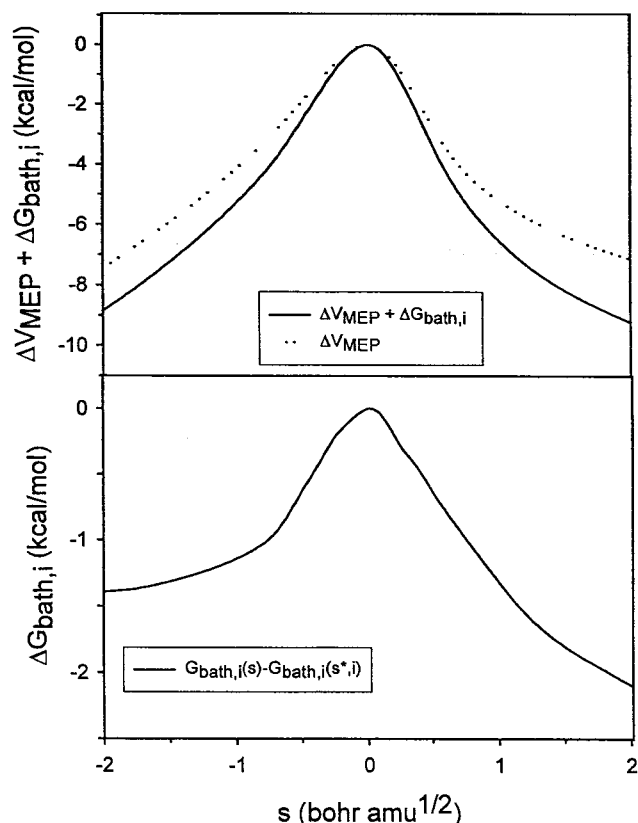


Figure 3. (top) Stage-2 (solid curve) and stage-3 effective potential of mean force used in microcanonical optimized multidimensional tunneling calculations, referenced to the value at the maximum, which is $s_{*,i}$. (bottom) Relative free energy change due to protein dynamics and fluctuation along the stage-2 reaction path for one of the bath configurations, i.e., $G_{bath,i}(s) - G_{bath,i}(s_{*,i})$.

TABLE 4: Computed Transmission Coefficients Averaged over Two Equilibrium Secondary-Zone Configurations (ESZ)

isotope	$\langle \Gamma^{(3)} \rangle$	$\langle \kappa^{(3)} \rangle$		$\langle \gamma^{(3)} \rangle$	
		ZCT	μ OMT	ZCT	μ OMT
HH	0.983	2.22	4.11	2.18	4.053
HT	0.982	1.98	3.28	1.948	3.23
DD	0.969	2.31	3.52	2.24	3.42
DT	0.960	2.12	3.365	2.04	3.24
TH	0.988	2.24	3.68	2.81	3.57
TD	0.990	2.17	3.51	2.145	3.47

from the simplest classical mechanical model to the most sophisticated theories in stage 2 and stage 3 calculations that include semiclassical tunneling corrections. Inclusion of the quantum mechanical vibrational energy lowers the CM free energy of activation by roughly 2 kcal/mol, leading to significant rate increase relative to the TST value from the classical mechanical PMF simulation. Quantum mechanical tunneling corrections further increase the rate by a factor of 2–3, depending on the specific isotope combinations. Since the effective potential barrier from the interpolated stage-3 bath free energy is narrower than the stage-2 potential (this results from the unsurprising peak of the bath free energy at the dynamical bottleneck, which could easily be anticipated as an entropic cost), the computed transmission coefficients are somewhat greater than the corresponding stage 2 values from both the ZCT and SCT approximation (Tables 3 and 4).

In the present article, we take the viewpoint that our final calculations, i.e., the stage-3 ones, are the most accurate. An

TABLE 5: Computed Rate Constants (1/s) for Six Isotopic Substitutions in the Hydride Transfer Reaction Catalyzed by LADH at 298 K

isotope	$k_{CVT/}^{SRC}$		$k_{CVT/}^{SSZ}$				$k_{CVT/}^{ESZ}$		
	CM	QC	QC	ZCT	μ OMT	ZCT	μ OMT	ZCT	μ OMT
stage (step) ^a	1(1)	1(2)	2(1)	2(2)	2(2)	2(2)	2(2)	3(2)	3(2)
note	b	c	c	c	c	d	d	d	d
HH	13.7	197	193	323	475	319	477	429	797
HT	13.7	182	178	275	375	271	376	354	588
DD	14.0	49.3	48.1	83	112	84	112	110	168
DT	14.0	48.3	47.2	80	107	81	107	99	156
TH	13.9	29.6	29.0	49	69	51	71	83	106
TD	13.9	27.9	27.4	45	63	46	64	60	97

^a Stage 1 has two steps, as described in the text. In the subsequent stages, we label the tunneling part as step 2. A heading containing CVT/ with ZCT below it denotes CVT/ZCT. ^b Umbrella sampling over a 50 ps run. ^c On the basis of 18 bath configurations from 2.5 to 50 ps. ^d On the basis of two configurations, in particular, those at 7.5 and 40 ps.

alternative viewpoint would be that the best estimate might lie somewhere between the stage-2 frozen-bath results and the stage-3 fully relaxed bath result.

5.3. Kinetic Isotope Effects (KIEs). Kinetic isotope effects, which are computed based on the rate constants listed in Table 5, along with the Swain–Schaad exponents, are given in Table 6. The Swain–Schaad exponents are defined as follows:

$$\alpha_{\text{prim}} = \frac{\ln(k_{\text{H}}^{\text{H}}/k_{\text{T}}^{\text{H}})}{\ln(k_{\text{D}}^{\text{D}}/k_{\text{T}}^{\text{D}})} \quad (23)$$

where the subscripts and superscripts of the rate constants in

$$\alpha_{\text{sec}} = \frac{\ln(k_{\text{H}}^{\text{H}}/k_{\text{H}}^{\text{T}})}{\ln(k_{\text{D}}^{\text{D}}/k_{\text{D}}^{\text{T}})} \quad (24)$$

eqs 23 and 24 indicate primary and secondary isotopes, respectively. The Swain–Schaad exponents have been used by previous workers^{114,115} as an indicator for tunneling to interpret experimental KIEs. In particular, if the Swain–Schaad exponents are greater than the nontunneling conventional-transition-state-theory limit of about 3.3, it is considered to be a strong indication of enhanced rate due to tunneling. For comparison, results obtained by the stage-1 CVT rate constants, which include quantized vibrations for the CM transition state and reactant state, are also listed in Table 6 along with SSZ and ESZ results with tunneling corrections. The experimental values in Table 6 are complicated by the fact that the hydride transfer step is not rate limiting in wild-type enzyme. Mutation experiments have been carried out to circumvent this problem, where the hydride transfer catalytic step is fully or more fully rate-limiting.^{4,6} Since X-ray structures of mutant enzymes, for example, the F93W mutant,⁷ are essentially superimposable with the wild-type protein, the underlying assumption is that the mutant enzymes have a similar mechanism for the catalytic step and thus provide a good indication of the intrinsic isotope effect of this reaction step.

Table 6 shows that the present calculations, like those in ref 22, qualitatively reproduce the nonclassical Swain–Schaad exponents found experimentally by Klinman and co-workers. The results from our stage-3 algorithm are particularly encouraging. Table 6 shows that the Swain–Schaad exponent is somewhat underestimated by the stage-3 ZCT calculations; we note, however, that the Swain–Schaad exponents are very

TABLE 6: Primary and Secondary Kinetic Isotope Effects and Exponents at 298 K

		SRC	SSZ			ESZ		expt ^a
		QC	QC	ZCT	μ OMT	ZCT	μ OMT	
primary ^b	$k_{\text{H}}^{\text{H}}/k_{\text{T}}^{\text{H}}$	6.63	6.67	6.55	6.86	5.15	7.54	7.1 (7.3–7.8)
	$k_{\text{D}}^{\text{D}}/k_{\text{T}}^{\text{D}}$	1.77	1.76	1.84	1.79	1.84	1.74	1.9 (1.8–1.9)
secondary ^b	$k_{\text{H}}^{\text{H}}/k_{\text{H}}^{\text{T}}$	1.081	1.087	1.176	1.265	1.21	1.36	1.33 (1.31–1.32)
	$k_{\text{D}}^{\text{D}}/k_{\text{D}}^{\text{T}}$	1.020	1.019	1.040	1.048	1.12	1.08	1.07 (1.03–1.05)
exponent	α_{prim}	3.3	3.4	3.2	3.3	2.7	3.6	3.1 (3.3)
	α_{sec}	3.8	4.4	4.1	5.0	1.7	4.2	4.1 (6.1–8.5)

^a References 4 and 5. Wild-type value is shown first followed by values for mutants in parentheses. ^b Notation: $k_{\text{primary}}^{\text{secondary}}$.

sensitive to precision, and the stage-3 transmission coefficients are averaged using only two reaction paths to keep the number of costly free energy perturbation calculations at a minimum; this may be insufficient. A similar comment about sensitivity of the Swain–Schaad exponents to the precision of the rate constants applies to the CVT/QC–SSZ value of α_{sec} , which is 4.4. At first glance, this is surprisingly large for a calculation that does not include tunneling. However, if we increase $k_{\text{D}}^{\text{D}}/k_{\text{D}}^{\text{T}}$ from 1.019 to 1.026, α_{sec} drops to 3.3. Such a small increase (0.7%) in the secondary KIE can be accomplished by increasing the final value of $\Delta G_{\text{act,T}}$ for the DT case by 0.004 kcal/mol or by decreasing the final value of $\Delta G_{\text{act,T}}$ for the DD case by 0.004 kcal/mol. Consideration of this sensitivity should make one very cautious about overinterpreting the Swain–Schaad exponents for cases where any of the KIEs is very close to unity. It is better to emphasize that our final stage-3 μ OMT KIEs, which differ more from unity, are in very good agreement with experiment.

6. Conclusions

The present study explores the dynamics and mechanism of the hydride transfer reaction from benzyl alcoholate to NAD⁺ in the active site of horse liver alcohol dehydrogenase (LADH) using a combined QM/MM simulation model and VTST. In this work, we describe a three-stage computational procedure that includes quantum mechanical tunneling and vibrational energy for computing the rate constants of enzymatic reactions. The new method builds upon two recent preliminary studies and formulates the rate constant within the new static-secondary-zone (SSZ) approximation and the new equilibrium-secondary-zone (ESZ) approximation in terms of a configurationally averaged transmission coefficient. First, we determine the potential of mean force for the enzymatic process with the inclusion of quantum mechanical vibrational energy, which leads to the canonical variational theory rate constant. Then, stage-2 is based on the SSZ approximation, in which the secondary zone is represented by its static potential field, whose gradient is the force of the static protein–solvent environment surrounding the catalytic reaction center, called the primary zone. Finally, this is followed by stage 3, in which the ESZ transmission coefficient is evaluated with the equilibrium free energy of the secondary zone. The present procedure allows for Boltzmann averaging over an ensemble of reactant and transition state conformations. The method includes nonequilibrium polarization effects in two ways: first of all, the protein and solvent need not be assumed to equilibrate to the primary zone, and secondly, even in the ESZ approximation, the protein and solvent enter into the reaction coordinate because the reaction coordinate for the transmission coefficient depends on the protein and solvent configuration at the secondary zone.

We use this method for semiclassical calculations of the reaction rate constants and kinetic isotope effects for oxidation of benzyl alcoholate to benzaldehyde by the horse liver alcohol dehydrogenase enzyme. The potential energy surface is modeled by a combined generalized hybrid orbital/quantum mechanical/molecular mechanical/valence bond (GHO-QM/MM/VB) method. The dynamics is treated by canonical variational-transition-state theory with the microcanonical optimized multidimensional tunneling (CVT/ μ OMT) approximation. The computed primary and secondary kinetic isotope effects are in accord with experimental studies by Klinman and co-workers. Furthermore, the present study shows that unless quantum mechanical tunneling effects are included in the computation of rate constants, the elevated Swain–Schaad exponent for the secondary KIE in LADH catalysis cannot be obtained. Thus, our computations confirm the experimental contention that the large Swain–Schaad exponent for secondary KIEs in the hydride transfer step of LADH is experimental evidence for hydrogen tunneling in enzymatic reactions.

Appendix

To calculate frequencies in a hypersurface normal to coordinate z , we must project the z direction out of the Hessian, which is the matrix of second derivatives of the potential with respect to the atomic Cartesian coordinates. Since the Hessian characterizes infinitesimal vibrations, it is sufficient to project out the z direction to first order. Therefore, the projected Hessian is^{99b}

$$\mathbf{H}^{\text{P}} = (\mathbf{1} - \mathbf{P})\mathbf{H}(\mathbf{1} - \mathbf{P}) \quad (\text{A1})$$

where

$$\mathbf{P} = \bar{\mathbf{b}}\bar{\mathbf{b}}^{\text{T}} \quad (\text{A2})$$

and

$$\bar{\mathbf{b}} \equiv \mathbf{b}/(\mathbf{b}^{\text{T}}\mathbf{b}) \quad (\text{A3})$$

Note that T denotes a transpose, \mathbf{b} is a column vector of order $3N_1$, and \mathbf{b}^{T} is a row vector of order $3N_1$. Therefore, \mathbf{P} , like the Hessian \mathbf{H} , is a $3N_1 \times 3N_1$ matrix. However, $\mathbf{b}^{\text{T}}\mathbf{b}$ is a scalar. Clearly $\bar{\mathbf{b}}$ is a unit column vector of order $3N_1$ in the direction of \mathbf{b} , and \mathbf{b}^{T} is its transpose.

Let $r_{\alpha\gamma}$ be a Cartesian coordinate ($\gamma = 1, 2, 3$) of atom α , and let $R_{\alpha\beta}$ be an internuclear distance. To calculate the potential of mean force along the distinguished reaction coordinate z for $\text{XA} - \text{B} + \text{CY} \rightarrow \text{XA} + \text{B} - \text{CY}$, we have

$$\begin{aligned} z &= R_{\text{AB}} - R_{\text{BC}} \\ &= [\sum_{\gamma} (r_{\text{A}\gamma} - r_{\text{B}\gamma})^2]^{1/2} - [\sum_{\gamma} (r_{\text{B}\gamma} - r_{\text{C}\gamma})^2]^{1/2} \end{aligned} \quad (\text{A4})$$

$$b_{Ay} = \frac{\partial z}{\partial r_{Ay}} = \frac{r_{Ay} - r_{By}}{R_{AB}} \quad (A5)$$

$$b_{By} = \frac{\partial z}{\partial r_{By}} = \frac{r_{By} - r_{Ay}}{R_{AB}} + \frac{r_{Cy} - r_{By}}{R_{BC}} \quad (A6)$$

$$b_{Cy} = \frac{\partial z}{\partial r_{Cy}} = \frac{r_{By} - r_{Cy}}{R_{BC}} \quad (A7)$$

$$b_{Dy} = 0, \quad D \neq A \text{ or } B \text{ or } C \quad (A8)$$

The vibrational frequencies (in units of radians per unit time) of the projected motion are given by

$$\omega_m = \lambda_m^{1/2} \quad (A9)$$

where λ_m is an eigenvalue of the mass-weighted force constant matrix **F** with elements¹⁴⁴

$$F_{ij} = (m_i m_j)^{-1/2} H_{ij}^P \quad (A10)$$

Alternatively, to carry out the calculation with the Hessian in mass-weighted coordinates, one could include the mass factors in **b**.

Acknowledgment. This work was supported in part by the National Science Foundation and by the National Institutes of Health.

References and Notes

- (1) Bibbs, J. A.; Demuth, H.-U.; Huskey, W. P.; Mordy, C. W.; Schowen, R. L. *J. Mol. Catal.* **1988**, *47*, 187.
- (2) Cha, Y.; Murray, C. J.; Klinman, J. P. *Science* **1989**, *243*, 1325.
- (3) Rucker, J.; Cha, Y.; Jonsson, T.; Grant, K. L.; Klinman, J. P. *Biochemistry* **1992**, *31*, 11489.
- (4) Bahnson, B. J.; Park, D.-H.; Kim, K.; Plapp, B. V.; Klinman, J. P. *Biochemistry* **1993**, *32*, 5503.
- (5) Bahnson, B. J.; Klinman, J. P. *Methods Enzymol.* **1995**, *249*, 373.
- (6) Kohen, A.; Klinman, J. P. *Acc. Chem. Res.* **1998**, *31*, 397.
- (7) Bahnson, B. J.; Colby, T. D.; Chin, J. K.; Goldstein, B. M.; Klinman, J. P. *Proc. Natl. Acad. Sci. U.S.A.* **1997**, *94*, 12797.
- (8) Rucker, J.; Klinman, J. P. *J. Am. Chem. Soc.* **1999**, *121*, 1997.
- (9) Rickert, K. W.; Klinman, J. P. *Biochemistry* **1999**, *38*, 12218.
- (10) Kohen, A.; Cannio, R.; Bartolucci, S.; Klinman, J. P. *Nature* **1999**, *399*, 496.
- (11) Kohen, A.; Klinman, J. P. *Chem. Biol.* **1999**, *6*, R191.
- (12) Chin, J. K.; Klinman, J. P. *Biochemistry* **2000**, *39*, 1278.
- (13) Borgis, D.; Hynes, J. T. In *The Enzyme Catalysis Process*; Cooper, A., Houben, J. L., Chien, L. C., Eds.; Plenum: New York, 1989; p 293.
- (14) Hwang, J. K.; Chu, Z. T.; Yadav, A.; Warshel, A. *J. Phys. Chem.* **1991**, *95*, 8445.
- (15) Hwang, J.-K.; Warshel, A. *J. Am. Chem. Soc.* **1996**, *118*, 11745.
- (16) Bruno, W. J.; Bialek, W. *Biophys. J.* **1992**, *63*, 689.
- (17) Alston, W. C. II; Kanska, M.; Murray, C. J. *Biochemistry* **1996**, *35*, 12873.
- (18) (a) Antoniou, D.; Schwarz, S. D. *Proc. Natl. Acad. Sci. U.S.A.* **1997**, *94*, 12360. (b) Antoniou, D.; Schwartz, S. D. *J. Chem. Phys.* **1998**, *108*, 3620.
- (19) Malmström, B. G. *J. Biol. Inorg. Chem.* **1998**, *339*.
- (20) Bala, P.; Grochowski, P.; Lesyng, B.; McCammon, J. A. *Ber. Bunsen-Ges., Phys. Chem.* **1998**, *102*, 580.
- (21) Alhambra, C.; Gao, J.; Corchado, J. C.; Villà, J.; Truhlar, D. G. *J. Am. Chem. Soc.* **1999**, *121*, 2253.
- (22) Alhambra, C.; Corchado, J. C.; Sánchez, M. L.; Gao, J.; Truhlar, D. G. *J. Am. Chem. Soc.* **2000**, *122*, 8197.
- (23) Garcia-Viloca, M.; Alhambra, C.; Truhlar, D. G.; Gao, J. *J. Chem. Phys.* **2001**, *114*, 9953.
- (24) Karsten, W. E.; Hwang, C.-C.; Cook, P. F. *Biochemistry* **1999**, *38*, 4398.
- (25) Brooks, H. B.; Jones, L. H.; Davidson, V. L. *Biochemistry* **1993**, *32*, 2725.
- (26) (a) Basran, J.; Sutcliffe, M. J.; Scrutton, N. S. *Biochemistry* **1999**, *38*, 3218. (b) Scrutton, N. S. *Biochem. Soc. Trans.* **1999**, *27*, 767.
- (27) Scrutton, N. S.; Basran, J.; Sutcliffe, M. J. *Eur. J. Biochem.* **1999**, *264*, 666.
- (28) Harris, R. J.; Meskys, R.; Sutcliffe, M. J.; Scrutton, N. S. *Biochemistry* **2000**, *39*, 1189.
- (29) Sutcliffe, M. J.; Scrutton, N. S. *Trends Biochem. Sci.* **2000**, *25*, 405.
- (30) Basran, J.; Patel, S.; Sutcliffe, M. J.; Scrutton, N. S. *J. Biol. Chem.* **2001**, *276*, 6234.
- (31) Kuznetsov, A. M.; Ulstrup, J. *Can. J. Chem.* **1999**, *77*, 1085.
- (32) Billeter, S. R.; Webb, S. P.; Iordanov, T.; Agarwal, P. K.; Hammes-Schiffer, S. *J. Chem. Phys.* **2001**, *114*, 6925.
- (33) Vieth, M.; Hirst, J. D.; Brooks, C. L. III, *J. Comput.-Aided Mol. Des.* **1998**, *12*, 563.
- (34) Bruice, T. C.; Benkovic, S. J. *Biochemistry* **2000**, *39*, 6267.
- (35) Kirkwood, J. G. *J. Chem. Phys.* **1935**, *3*, 300.
- (36) Bennett, C. H. *ACS Symp. Ser.* **1977**, *46*, 63.
- (37) Chandler, D. *J. Chem. Phys.* **1978**, *68*, 2959.
- (38) (a) Chandrasekhar, J.; Smith, S. F.; Jorgensen, W. L. *J. Am. Chem. Soc.* **1984**, *106*, 3049. (b) Lim, D.; Jensen, C.; Repasky, M. P.; Jorgensen, W. L. *ACS Symp. Ser.* **1999**, *721*, 74.
- (39) Hynes, J. T. In *Theory of Chemical Reaction Dynamics*; Baer, M., Ed.; CRC Press: Boca Raton, FL, 1985; Vol. 4, p 171.
- (40) Case, D. A.; McCammon, J. A. *Ann. N.Y. Acad. Sci.* **1986**, *482*, 222.
- (41) Berne, B. J.; Borkovic, M.; Straub, J. E. *J. Phys. Chem.* **1988**, *92*, 3711.
- (42) G. Cicotti, M. Ferrario, J. R. Hynes, and, R. Kapral, *J. Chem. Phys.* **1990**, *93*, 7137.
- (43) Keirstad, W. P.; Wilson, K. R.; Hynes, J. T. *J. Chem. Phys.* **1991**, *95*, 5256.
- (44) Field, M. J. In *Computer Simulation of Biomolecular Systems*; van Gunsteren, W. F.; Weiner, P. K.; Wilkinson, A. J., Eds.; ESCOM: Leiden, 1993; Vol. 2, p 82.
- (45) Truhlar, D. G.; Liu, Y.-P.; Schenter, G. K.; Garrett, B. C. *J. Phys. Chem.* **1994**, *98*, 8396.
- (46) Schenter, G. K.; Garrett, B. C. *Int. Rev. Phys. Chem.* **1994**, *13*, 263.
- (47) Hinsen, K.; Roux, B. *J. Chem. Phys.* **1997**, *106*, 3567.
- (48) M. Sprik and, G. Cicotti, *J. Chem. Phys.* **1998**, *109*, 7737.
- (49) Berne, B. J.; Borkovec, M. *J. Chem. Soc., Faraday Trans.* **1998**, *94*, 2717.
- (50) Pliego, J. R., Jr.; De Almeida, W. B. *Phys. Chem. Chem. Phys.* **1999**, *1*, 1031.
- (51) (a) Gao, J. *Acc. Chem. Res.* **1996**, *29*, 298. (b) Wu, N.; Mo, Y.; Gao, J.; Pai, E. F. *Proc. Natl. Acad. Sci. U.S.A.* **2000**, *97*, 2017.
- (52) Schatz, G. C.; Ratner, M. A. *Quantum Mechanics in Chemistry*; Prentice Hall: Englewood Cliffs, NJ, 1993; pp 167–172.
- (53) Miller, W. H. *Adv. Chem. Phys.* **1974**, *25*, 69.
- (54) Karplus, M.; Porter, R. N.; Sharma, R. D. *J. Chem. Phys.* **1965**, *43*, 3259.
- (55) Karplus, M. *Discuss. Faraday Soc.* **1967**, *44*, 76.
- (56) Schatz, G. C.; Ter Horst, M.; Takayangi, T. In *Modern Methods for Multidimensional Dynamics Computations in Chemistry*; Thompson, D. L., Ed.; World Scientific: Singapore, 1998; p 1.
- (57) Walsh, C. *Enzyme Reaction Mechanisms*; W. H. Freeman: New York, 1979.
- (58) Fersht, A. *Structure and Mechanism in Protein Science*; W. H. Freeman: New York, 1999; Chapters 8 and 16.
- (59) Brooks, B. R.; Bruccoleri, R. E.; Olafson, B. D.; States, D. J.; Swaminathan, S.; Karplus, M. *J. Comput. Chem.* **1983**, *4*, 187.
- (60) Keck, J. C. *Discuss. Faraday Soc.* **1962**, *33*, 173.
- (61) Anderson, J. B. *J. Chem. Phys.* **1975**, *62*, 2446.
- (62) Miller, W. H. *J. Chem. Phys.* **1974**, *61*, 1823.
- (63) Garrett, B. C.; Truhlar, D. G. *J. Phys. Chem.* **1979**, *83*, 1052.
- (64) Truhlar, D. G.; Isaacson, A. D.; Garrett, B. C. In *Theory of Chemical Reaction Dynamics*; CRC Press: Boca Raton, FL, 1985; Vol. IV, p 65.
- (65) Truhlar, D. G.; Garrett, B. C. *Faraday Discuss. Chem. Soc.* **1987**, *84*, 464.
- (66) Neria, E.; Karplus, M. *Chem. Phys. Lett.* **1997**, *267*, 23.
- (67) Alhambra, C.; Corchado, J. C.; Sánchez, M. L.; Villà, J.; Gao, J.; Truhlar, D. G. CHARMMRATE, version 1.0 (a module of CHARMM, version 27).
- (68) Lu, D.-h.; Truong, T. N.; Melissas, V. S.; Lynch, G. C.; Liu, Y.-P.; Garrett, B. C.; Steckler, R.; Isaacson, A. D.; Rai, S. N.; Hancock, G. C.; Lauderdale, J. G.; Joseph, T.; Truhlar, D. G. *Comput. Phys. Commun.* **1992**, *71*, 235.
- (69) (a) Steckler, R.; Hu, W.-P.; Liu, Y.-P.; Lynch, G. C.; Garrett, B. C.; Isaacson, A. D.; Lu, D.-h.; Melissas, V. S.; Truhlar, D. G. *Comput. Phys. Commun.* **1995**, *88*, 344. (b) Chuang, Y.-Y.; Corchado, J. C.; Fast, P. L.; Villà, J.; Hu, W.-P.; Liu, Y.-P.; Lynch, G. C.; Nguyen, K. A.; Jackels, C. F.; Gu, M. Z.; Rossi, I.; Coitiño, E. L.; Clayton, S.; Melissas, V. S.; Steckler, R.; Garrett, B. C.; Isaacson, A. D.; Truhlar, D. G. POLYRATE, version 8.1.1; University of Minnesota: Minneapolis, MN, 1999.
- (70) Garrett, B. C.; Truhlar, D. G. *J. Am. Chem. Soc.* **1989**, *111*, 1232.
- (71) Garrett, B. C.; Truhlar, D. G. *J. Chem. Phys.* **1979**, *70*, 1593.

- (72) Garrett, B. C.; Truhlar, D. G.; Grev, R. S.; Magnuson, A. W. *J. Phys. Chem.* **1980**, *84*, 1749.
- (73) Truhlar, D. G.; Garrett, B. C. *Acc. Chem. Res.* **1980**, *13*, 440.
- (74) Isaacson, A. D.; Truhlar, D. G. *J. Chem. Phys.* **1982**, *76*, 1380.
- (75) Lauderdale, J. G.; Truhlar, D. G. *J. Chem. Phys.* **1986**, *84*, 1843.
- (76) Tucker, S. C.; Truhlar, D. G. In *New Theoretical Concepts for Understanding Organic Reactions*; Bertrán, J., Csizmadia, I. G., Eds.; NATO ASI Series C267; Kluwer: Dordrecht, 1989; p 291.
- (77) Truhlar, D. G.; Lu, D.-h.; Tucker, S. C.; Zhao, X. G.; González-Lafont, A.; Truong, T. N.; Maurice, D.; Liu, Y.-P.; Lynch, G. C. *ACS Symp. Ser.* **1992**, *502*, 16.
- (78) Liu, Y.-P.; Lu, D.-h.; González-Lafont, A.; Truhlar, D. G.; Garrett, B. C. *J. Am. Chem. Soc.* **1993**, *115*, 7806.
- (79) Liu, Y.-P.; Lynch, G. C.; Truong, T. N.; Lu, D.-h.; Truhlar, D. G.; Garrett, B. C. *J. Am. Chem. Soc.* **1993**, *115*, 2408.
- (80) Fernandez-Ramos, A.; Truhlar, D. G. *J. Chem. Phys.* **2001**, *114*, 1491.
- (81) Babamov, V. K.; Marcus, R. A. *J. Chem. Phys.* **1978**, *74*, 1790.
- (82) Garrett, B. C.; Truhlar, D. G.; Wagner, A. F.; Dunning, T. H. Jr. *J. Chem. Phys.* **1983**, *78*, 4400.
- (83) Kim, Y.; Truhlar, D. G.; Kreevoy, M. M. *J. Am. Chem. Soc.* **1991**, *113*, 7837.
- (84) Kim, Y.; Kreevoy, M. M. *J. Am. Chem. Soc.* **1992**, *114*, 7116.
- (85) Truhlar, D. G.; Garrett, B. C. *J. Chim. Phys.* **1987**, *84*, 365.
- (86) Truhlar, D. G.; Gordon, M. S. *Science* **1990**, *249*, 491.
- (87) Wonchoba, S. E.; Truhlar, D. G. *J. Chem. Phys.* **1993**, *99*, 9637.
- (88) Chuang, Y.-Y.; Cramer, C. J.; Truhlar, D. G. *Int. J. Quantum Chem.* **1998**, *70*, 887.
- (89) Chuang, Y.-Y.; Radhakrishnan, M. L.; Fast, P. L.; Cramer, C. J.; Truhlar, D. G. *J. Phys. Chem.* **1999**, *103*, 4893.
- (90) Truhlar, D. G.; Garrett, B. C. *J. Phys. Chem. B* **2000**, *104*, 1069.
- (91) (a) Torrie, G. M.; Valleau, J. P. *J. Chem. Phys.* **1977**, *23*, 187. (b) Valleau, J. P.; Torrie, G. M. In *Statistical Mechanics, Part A*; Berne, B. J., Ed.; Plenum: New York, 1977; p 137.
- (92) Kottalam, J.; Case, D. A. *J. Am. Chem. Soc.* **1988**, *110*, 7690.
- (93) Roux, B. *Computer Phys. Commun.* **1995**, *91*, 275.
- (94) Alhambra, C.; Wu, L.; Zhang, Z.-Y.; Gao, J. *J. Am. Chem. Soc.* **1998**, *120*, 3858.
- (95) Hill, T. L. *An Introduction to Statistical Thermodynamics*; Addison-Wesley: Reading, MA, 1960; p 313.
- (96) Mills, G.; Jónsson, H. *Phys. Rev. Lett.* **1994**, *72*, 1124.
- (97) Truhlar, D. G.; Garrett, B. C.; Klippenstein, S. J. *J. Phys. Chem.* **1996**, *100*, 12771.
- (98) Mielke, S. L.; Truhlar, D. G. *J. Chem. Phys.* **2001**, *115*, 652.
- (99) (a) Lu, D.-h.; Zhao, M.; Truhlar, D. G. *J. Comput. Chem.* **1991**, *12*, 376. (b) Lu, D.-h.; Truhlar, D. G. *J. Chem. Phys.* **1993**, *99*, 2723.
- (100) (a) Shavitt, I. *J. Chem. Phys.* **1968**, *49*, 4048. (b) Marcus, R. A. *J. Chem. Phys.* **1968**, *49*, 2610.
- (101) Truhlar, D. G.; Kuppermann, A. *J. Am. Chem. Soc.* **1971**, *93*, 1840.
- (102) Fukui, K. In *The World of Quantum Chemistry*; Daudel, R., Pullman, A., Eds.; Reidel: Dordrecht, The Netherlands, 1974; p 113.
- (103) Jorgensen, W. L.; Ravimohan, C. *J. Chem. Phys.* **1985**, *83*, 3050.
- (104) (a) McCammon, J. A.; Harvey, S. C. *Dynamics of Proteins and Nucleic Acids*; Cambridge University Press: Cambridge, 1987. (b) *Computer Simulation of Biomolecular Systems*; van Gunsteren, W. F., Weiner, P. K., Wilkinson, A. J., Eds.; ESCOM: Leiden, 1993; Vol. 2.
- (105) Gao, J.; Kuczera, K.; Tidor, B.; Karplus, M. *Science* **1989**, *244*, 1069.
- (106) Chuang, Y.-Y.; Corchado, J. C.; Truhlar, D. G. *J. Phys. Chem. A* **1997**, *103*, 1140.
- (107) Hu, W.-P.; Liu, Y.-P.; Truhlar, D. G. *J. Chem. Soc., Faraday Trans.* **1994**, *90*, 1715.
- (108) Schmidt, J.; Chen, J.; DeTraglia, M.; Minkel, D.; McFarland, J. T. *J. Am. Chem. Soc.* **1979**, *101*, 3624.
- (109) Cook, P. F.; Cleland, W. W. *Biochemistry* **1981**, *20*, 1805.
- (110) Kvassman, J.; Larsson, A.; Pettersson, G. *Eur. J. Biochem.* **1981**, *114*, 555.
- (111) Sekhar, V. C.; Plapp, B. V. *Biochemistry* **1990**, *29*, 4289.
- (112) Shearer, G. L.; Kim, K.; Lee, K. M.; Wang, C. K.; Plapp, B. V. *Biochemistry* **1993**, *32*, 11186.
- (113) Cook, P. F.; Blanchard, J. S.; Cleland, W. W. *Biochemistry* **1980**, *19*, 4853.
- (114) Swain, C. G.; Stivers, E. C.; Reuwer, J. F. Jr.; and Schaad, L. J. *J. Am. Chem. Soc.* **1958**, *80*, 5885.
- (115) Saunders, W. H., Jr. *J. Am. Chem. Soc.* **1985**, *107*, 164.
- (116) Schneider, M. E.; Stern, M. J. *J. Am. Chem. Soc.* **1972**, *94*, 1517.
- (117) Eklund, H.; Plapp, B. V.; Samana, J.-P.; Brändén, C.-I. *J. Biol. Chem.* **1982**, *257*, 14349.
- (118) Ramaswamy, S.; Eklund, H.; Plapp, B. V. *Biochemistry* **1994**, *33*, 5230.
- (119) Deng, H.; Schindler, J. F.; Berst, K. B.; Plapp, B. V.; Callender, R. *Biochemistry* **1998**, *37*, 14267.
- (120) Bash, P. A.; Field, M. J.; Karplus, M. *J. Am. Chem. Soc.* **1987**, *109*, 8092.
- (121) (a) Gao, J. *Rev. Comput. Chem.* **1995**, *7*, 119. (b) Gao, J.; Xia, X. *Science* **1992**, *258*, 631.
- (122) *Combined Quantum Mechanical and Molecular Mechanical Methods*; Gao, J., Thompson, M. A., Eds.; ACS Symposium Series 712; American Chemical Society: Washington, DC, 1998.
- (123) Gao, J.; Amara, P.; Alhambra, C.; Field, M. J. *J. Phys. Chem. A* **1998**, *102*, 4714.
- (124) Dewar, M. J. S.; Zoebisch, E. G.; Healy, E. F.; Stewart, J. J. P. *J. Am. Chem. Soc.* **1985**, *107*, 3902.
- (125) Dewar, M. J. S.; Yuan, Y. C. *Inorg. Chem.* **1990**, *29*, 3881.
- (126) Dewar, M. J. S.; Merz, K. M. *Organometallics* **1988**, *7*, 522.
- (127) London, F. Z. *Elektrochem.* **1929**, *35*, 552.
- (128) Eyring, H.; Polanyi, M. Z. *Phys. Chem.* **1931**, *B12*, 279.
- (129) Sato, S. *J. Chem. Phys.* **1955**, *23*, 592.
- (130) Polanyi, J. C. *J. Quant. Spectrosc. Radiat. Transfer* **1963**, *3*, 471.
- (131) MacKerell, A. D., Jr.; Bashford, D.; Bellot, M.; Dunbrack, R. L.; Field, M. J.; Fischer, S.; Gao, J.; Guo, H.; Ha, S.; Joseph-McCarthy, D.; Kuchnir, L.; Kuczera, K.; Lau, F. T. K.; Mattos, C.; Michnick, S.; Ngo, T.; Nguyen, D. T.; Prodhom, B.; Reiher, W. E. III; Roux, B.; Schlenkerich, M.; Smith, J. C.; Stote, R.; Straub, J.; Watanabe, M.; Wiorkiewicz-Kuczera, J.; Yin, D.; Karplus, M. *J. Phys. Chem. B* **1998**, *102*, 3586.
- (132) Stote, R. H.; Karplus, M. *Proteins: Struct., Funct., Genet.* **1995**, *23*, 12.
- (133) Paverlites, J. J.; Gao, J.; Bash, P. A.; Mackerell, A. D., Jr. *J. Comput. Chem.* **1997**, *18*, 221.
- (134) Jorgensen, W. L.; Chandrasekhar, J.; Madura, J. D.; Impey, R. W.; Klein, M. L. *J. Chem. Phys.* **1983**, *79*, 926.
- (135) Brooks, C. L.; Brunger, A.; Karplus, M. *Biopolymers* **1985**, *24*, 843.
- (136) Ryckaert, J.-P.; Cicotti, G.; Berendsen, H. J. C. *J. Comput. Phys.* **1977**, *23*, 327.
- (137) Brooks, C. L.; III; Pettit, B. M.; Karplus, M. *J. Chem. Phys.* **1985**, *83*, 5897.
- (138) Gao, J. *J. Phys. Chem.* **1992**, *96*, 537.
- (139) Gao, J. *J. Mol. Struct. (THEOCHEM)* **1996**, *370*, 203.
- (140) Villà, J.; Truhlar, D. G. *Theor. Chem. Acc.* **1997**, *97*, 317.
- (141) González-Lafont, A.; Lluch, J. M.; Bertrán, J.; Steckler, R.; Truhlar, D. G. *J. Phys. Chem. A* **1998**, *102*, 3420.
- (142) Almarsson, O.; Karaman, R.; Bruice, T. C. *J. Am. Chem. Soc.* **1992**, *114*, 8702.
- (143) Luo, J.; Kah, K.; Bruice, T. C. *Bioorg. Chem.* **1999**, *27*, 289.
- (144) Levine, I. N. *Quantum Chemistry*, 5th ed.; Prentice Hall: Upper Saddle River, NJ, 1991; p 546.